

Understanding AuPd Alloy Nanoparticle Structure under Vacuum Using DFT and Monte Carlo Methods

Conor Waladt, Rajeev Kumar, and David Hibbitts*

Cite This: *J. Phys. Chem. C* 2025, 129, 5702–5717

Read Online

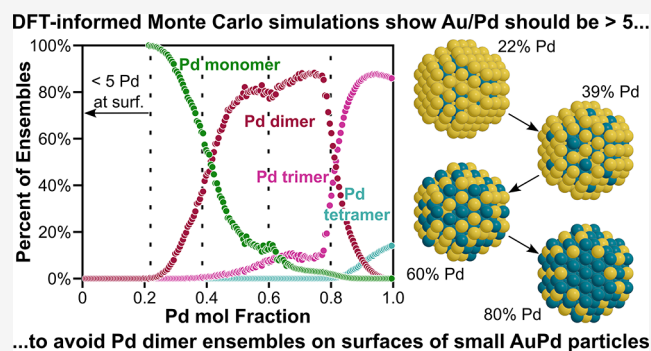
ACCESS |

Metrics & More

Article Recommendations

Supporting Information

ABSTRACT: AuPd is a miscible metal alloy that is often used in catalysis. Supported AuPd catalysts, at high Au/Pd ratios, form single-atom alloys (SAAs) that have been shown to enhance rates and/or selectivities for many catalytic reactions, including (de)-hydrogenations, hydrogenolysis, and C–C and C–O coupling reactions. While many computational studies have examined the stability of AuPd structures (the arrangement of atoms within the miscible alloy), most focused on generic alloys rather than SAAs and those that have closely investigated SAAs focused on single crystal surfaces. In this work, we use density functional theory (DFT) to calculate exchange energies (swapping an Au atom with a Pd atom) in a 201-atom truncated octahedral nanoparticle model with a focus on particles with high Au/Pd ratios. We calculate these exchange energies as a function of Pd location within the nanoparticle, the number of Pd atoms neighboring and near those exchange sites, and the total Pd content in the nanoparticle. These DFT-calculated exchange energies are also used to inform simple physics-based models (in contrast to cluster expansion or neural network models) that show good agreement with DFT-calculated values with relatively few regressed parameters. These models are then implemented into Monte Carlo (MC) simulations to predict the nanoparticle structure as a function of composition and temperature. The results show that Pd prefers to be in the subsurface of nanoparticles and that Pd prefers to be isolated from itself within Au. Both observations agree well with prior experimental and computational studies of single-crystal systems. We also show that the overall composition of the nanoparticle influences exchange energies by changing the electronic properties (e.g., Fermi level) of the system, which is relevant as Pd has one fewer valence electron than Au. MC simulations show that, in a vacuum, Pd begins to populate the surface of these ~2 nm nanoparticles at around 20 mol % Pd (at 298 K) and that the number of Pd surface monomers, desired for SAA applications, goes through a maximum near 40 mol % Pd. As the temperature increases, Pd is more prevalent at the surface, but the influence of temperature is relatively muted. While AuPd structures are known to change in the presence of reactive gases (e.g., CO or O₂), these studies characterize the baseline thermodynamic arrangements that can be used to understand surface restructuring during catalyst characterization and reaction studies.



1. INTRODUCTION

Bimetallic alloys can combine the catalytic properties of two metals to form a better catalyst than either metal in their monometallic form.¹ This holds true for single-atom alloys (SAAs) that are typically comprised of a highly active metal, like a Pt-group metal (e.g., Pt, Pd, Ir), dispersed in a less active metal, like the coinage metals (Cu, Ag, Au).^{1–5} SAAs have been studied for catalyzing a variety of reactions, including but not limited to selective hydrogenations,^{1,5–15} hydrogenolysis,^{1,16–19} dehydrogenations,^{1,16,20–32} C–C and C–O coupling reactions,^{1,11,33–38} and oxidation/reduction reactions.^{1,7,39–49} They potentially provide catalytic improvements in activity and selectivity along with resistance to deactivation via coking or CO poisoning.^{1,11,33,34,38}

One of the SAA catalysts that has been well-studied is AuPd, where Pd is present in low concentrations, and these have been studied for many applications. For example, AuPd/TiO₂

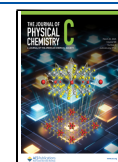
particles can oxidize methane to methanol (323 K, 30.5 bar).^{26,45} AuPd SAA catalysts were shown to provide great activity and durability for coupling reactions of aryl halides (353 K).^{1,37} AuPd(100) single crystals with SAA behavior have been shown to support low-temperature CO oxidation (<400 K, 1.0 × 10^{−3} Torr).^{1,44} SAA AuPd/SiO₂ catalysts can improve selectivities toward desired alkenes (over undesired alkanes) during the hydrogenations of 1-hexyne (5 bar H₂, 1% hexyne, 100–363 K)^{6,9,11} and acetylene (1% C₂H₂, 298–523 K).^{8,13}

Received: December 18, 2024

Revised: January 21, 2025

Accepted: January 22, 2025

Published: March 5, 2025



When Pd is dispersed on small Au particles (~ 2 nm), the ring-opening hydrogenolysis of 5-hydroxymethylfuran can be achieved (10 bar, 393 K).¹⁶ A variety of AuPd catalysts (including SAA to 1 monolayer [ML] Pd) were investigated both computationally and experimentally (1.0×10^{-10} Torr, 77–500 K) for the selective dehydrogenation (and subsequent decomposition) of ethanol.^{23,24,27,28} Several computational and experimental studies show that AuPd alloy catalysts inhibit the decomposition of alkanes and alkenes to coke, which is often seen on Pd-based catalysts.^{11,33,34,38} Finally, AuPd single-atom sites have been shown to promote reduction reactions, in particular, the reduction of O_2 in the direct synthesis of hydrogen peroxide (0.50–0.55 bar H_2 , 0.50–0.60 bar O_2 , 200–313 K).^{43,47–52} The advantage of using SAA AuPd catalysts for H_2O_2 synthesis is that these single-atom active sites are able to molecularly bind O_2 , preserving the O–O bond and thus avoiding undesired H_2O formation, while also providing greater activity than pure Au.^{39–42} In all of these cases, AuPd alloys provided greater activity and/or selectivity for the given reactions than what could be achieved using either monometallic Au or monometallic Pd.

Understanding the structure of AuPd materials is important for catalyst design. Single-crystal density functional theory (DFT) calculations showed that moving isolated surface Pd atoms next to each other to form Pd ensembles is endothermic for both Pd dimers (7 kJ mol⁻¹) and Pd trimers (17 kJ mol⁻¹).⁵³ Similar calculations showed that exchanging Au for Pd becomes more difficult as the number of neighboring Au increases, further suggesting that Pd prefers to be isolated.⁵⁴ These calculations were corroborated by CO–DRIFTS spectroscopy (303 K, 0.1 bar) after H_2 reduction (473 K)⁵³ and infrared reflection-adsorption spectroscopy (IRAS) of similar materials under ultrahigh vacuum (1.0×10^{-10} Torr, 80–400 K)⁵⁵ conditions, with both showing no peaks indicative of Pd clusters (~ 1940 – 1805 cm⁻¹). DFT calculations also showed that moving a surface Pd to the subsurface is exothermic (-35 kJ mol⁻¹), suggesting that the subsurface is the preferred location for Pd in a vacuum.^{53,54} This preference for Pd to be in the subsurface is corroborated by IRAS on AuPd materials that started as 5 ML of Pd deposited onto Au. After annealing at 600 K in an inert atmosphere, the peaks corresponding to Pd ensembles got smaller, and after annealing at 800 K, the peaks completely disappeared and a peak for atop Au appeared, suggesting that most of the Pd moved to the subsurface, leaving just isolated Pd at the surface.⁵⁵ Temperature-programmed desorption of CO on Pd-dominant materials also showed that Au will tend to stay at the surface of the particles as peaks associated with CO desorbing from Pd (~ 450 K) rapidly lost intensity with increasing Au content.⁵⁶ These prior experimental and computational data suggest that Pd naturally prefers to be in the subsurface of Au and is isolated from itself. However, adsorbates, such as CO*, can cause restructuring of the nanoparticle to bring Pd to the surface, as confirmed by CO–DRIFTS and DFT studies.^{53,57} This effect is driven by the fact that CO binds much stronger to Pd than Au and will therefore restructure AuPd materials to form Pd–C bonds when possible, resulting in different arrangements of Pd atoms than would be expected under vacuum. These prior studies, however, have focused on single-crystal materials (by DFT⁵³ or in UHV^{55,56} studies) or on large SAA nanoparticles (4.1–7.6 nm diameter)^{53,57} where low-index facets are expected to be dominant. There are studies that have investigated smaller

nanoparticles (1–8 nm). Experimentally, it has been shown that you can make a $Au_{core}Pd_{shell}$ particle, but as you increase the temperature to above 500 K, Au comes to the surface and Pd migrates to the subsurface, approaching an $Au_{shell}Pd_{core}$.^{58,59} These Pd-shell materials are likely possible because at low temperatures, the particles can be kinetically trapped. Computational studies using a variety of techniques on smaller nanoparticles also show that Au prefers to be at the surface and Pd prefers the subsurface,^{58–66} agreeing with the single-crystal studies previously discussed. These studies also note that at lower Pd contents ($\sim 25\%$ Pd), there is a low Pd–Pd coordination, suggesting Pd prefers to be isolated from itself, again agreeing with other studies.^{61,62} However, these smaller particle studies focus on general alloys rather than SAAs. Unfortunately, large AuPd SAA nanoparticles will be limited in practice by the inefficiency of such nanoparticles (low dispersions) and the high cost of Au. One goal within this area is to synthesize small AuPd nanoparticles with greater Pd content (without decreasing performance) to maximize the active-site per Au ratio and, thus, minimize cost.

Alloys, even SAAs, introduce a vast configurational space of what catalyst particles and surfaces could look like. One method that is used to sample this large configurational space is Monte Carlo (MC) simulations. Many studies of SAAs and reactions promoted by them, including AuPd, have employed MC methods to better our understanding of a given structure or reaction.^{51,52,54,67–72} The majority of these studies use DFT calculations of single-crystal surfaces to inform different prediction models for MC simulations. A cluster expansion model is often used as a prediction model; it works by assigning a “pseudospin” variable to each atom in clusters. For example, a pair cluster consists of two neighboring metal atoms and would have a combined spin value of 1, -1 , and 1 as the composition of the pair varied across AuAu, AuPd, and PdPd structures. These cluster values are then multiplied by cluster interaction parameters, which are fit to DFT training data.^{52,70–73} These methods can generate large (10^2 – 10^3) numbers of parameters for even simple systems, depending on the number of clusters involved, and have been shown to generate accurate system energy predictions. Canonical MC simulations using a cluster expansion model (in two dimensions) have been done for AuPd(111) and AuPd(100) surfaces, and the results show that Pd prefers heteronuclear (Pd–Au) interactions and will predominantly form monomers and dimer ensembles.⁷⁰ These data agree with other prior computational and experimental studies (discussed above) that indicate Pd prefers to be isolated/highly dispersed within Au.^{53,55,61,62} Another possible model that can be used is a neural network, for instance, one trained on 3914 DFT calculations was developed to predict energies of AuPd(111) surface alloys.⁶⁹ MC simulations performed using this model predicted segregation of Au to the surface was consistently favorable.⁶⁹ Some studies have used molecular dynamics to inform MC simulations of AuPd particles.^{61,62} These investigations focused primarily on the geometry of the nanoparticles but did observe that Au tended to move to the surface.^{53,55,56,58,59,62–66} An embedded-atom model (EAM) was used to inform another MC study that looked at a variety of particle sizes ranging from 55 to 5083 atoms and 3 different AuPd compositions.⁶² Finally, a physical model can be used to perform MC simulations. A model developed for AuPd surface alloys used the numbers of Pd and Au atoms and the number of each type of unique M–M bond (e.g., an interaction of Pd–

Au could have both atoms at the surface, one at the surface and the other in the subsurface, or both in the subsurface for a total of 4 unique bonds). Energies of the AuPd alloys were predicted with good agreement with DFT using this model in MC simulations.⁵⁴ While those prior studies of surfaces and nanoparticles consistently show that Au prefers to be at the surface, the underlying methods require a large number of parameters (cluster expansion), a large training set (neural networks), or using force fields or semiempirical (EAM) methods.

In this work, we perform DFT calculations on AuPd particle models to extend and parameterize physics-based models (with few parameters) that can then be used to inform MC simulations of AuPd nanoparticles. DFT calculations give insights into how Pd–Au exchange energies are influenced by exchange site, composition of first and second coordination shells, and overall composition of the nanoparticle. We show that exchange energies can be fit with physics-based models featuring as few as three regressed parameters. MC simulation results agree well with the reported literature in that we predict Pd to prefer subsurface positions (Au dominates the surface) and that Pd will remain isolated from itself. Here, we focus on the structure of AuPd particles under vacuum conditions to establish a baseline while recognizing that surface restructuring is expected in the presence of many reaction environments.

2. COMPUTATIONAL METHODS

2.1. Density Functional Theory. Periodic DFT calculations were implemented within the Computational Catalysis Interface (CCI)⁷⁴ and were performed using the Vienna *ab initio* simulation package (VASP).^{75–78} The wave functions were constructed using plane waves with a 400 eV energy cutoff, while the projector augmented wave (PAW) method was used to describe the wave functions in the core region.^{79,80} The revised Perdew–Burke–Ernzerhof (RPBE)^{81–83} functional form of the generalized gradient approximation (GGA) was used for most DFT calculations performed in this work, with other exchange–correlation functionals examined in select cases: PBE,⁸² PBE-D3BJ,^{84,85} PBEsol,⁸⁶ RPBE-D3BJ,^{84,85} optB880vdW,^{87–90} optB86b-vdW,^{87–89} and vdW-DF2.^{87–89,91}

DFT calculations examined bulk crystals, single-crystal surfaces, and polycrystalline nanoparticles. Bulk structures were modeled using the conventional fcc unit cell comprised of 4 atoms. These calculations were done in three steps, as this multistep process has been demonstrated to be 5–10 times faster than a single-step convergence for metal surface calculations.⁷⁴ The first step had wave functions converge to within 10^{-4} eV, and forces were calculated using an FFT grid $1.5\times$ the momentum cutoff. This step converged after the maximum force on each atom was <0.1 eV \AA^{-1} . The second step had wave functions converge to within 10^{-6} eV, and forces were calculated using an FFT grid $2\times$ the momentum cutoff. This step converged after the maximum force on each atom was <0.05 eV \AA^{-1} . The third step consisted of a single-point calculation. Bulk metal structures were performed using a $12 \times 12 \times 12$ k -point mesh. Spin polarization had no influence on the energies of these bulk structures (variations $<3 \times 10^{-3}$ eV for bulk structures), as expected.

Slab models were based on 4×4 Au(111) close-packed and Au(100) lattices with four layers in the orthogonal direction and a 10 \AA vacuum between slabs. These optimizations follow a three-step process similar to that for the bulk crystal calculations. The first step had wave functions converge to

within 10^{-4} eV, and forces were calculated using a fast Fourier transform (FFT) grid $1.5\times$ the momentum cutoff. The second step had wave functions converge to within 10^{-6} eV, and forces were calculated using an FFT grid $2\times$ the momentum cutoff. Both steps converged after the maximum force on each atom was <0.05 eV \AA^{-1} . The two structural optimizations were performed using $3 \times 3 \times 1$ sampling of the Brillouin zone. The third step consisted of a single-point calculation using an enlarged sampling of the Brillouin zone ($6 \times 6 \times 1$) with the same wave function criteria as the first step.

Particle models were constructed as a symmetric truncated octahedral particle with 201 atoms (~ 1.7 nm). Truncated octahedral particles have been shown to be one of the most stable particle geometries for fcc nanoparticles as they allow for large (111) facets to minimize formation energies while also avoiding highly strained corner atoms like in a normal octahedron.^{60,61,92–96} We chose the truncated octahedral particle because of its high symmetry. Truncated octahedral particles consist of eight hexagonal (111) terraces and six square (100) terraces connected by edge and corner atoms. The distribution of surface sites (e.g., corner and edge) and details of particles relevant to this study are shown in Table S1. For particle optimizations, a two-step process was used, like that described for the periodic slab calculations, with an increasing wave function convergence and a more accurate FFT grid in Step 2 than in Step 1. For both steps, the Brillouin zone was sampled only at the Γ -point. As many of these particles will have an odd number of electrons, we again tested the effects of spin polarization, and the results showed a negligible shift in energies $<2.2 \times 10^{-2}$ eV; therefore, spin polarization was not used for these calculations.

In addition to nanoparticle energies, we calculated electron affinities (EA):

$$EA = E[\text{Au}_x\text{Pd}_y^{-1}] - E[\text{Au}_x\text{Pd}_y] \quad (1)$$

and ionization energies (IE):

$$IE = E[\text{Au}_x\text{Pd}_y^{+1}] - E[\text{Au}_x\text{Pd}_y] \quad (2)$$

which are the differences required to add (EA) or remove (IE) an electron from the nanoparticle, respectively. These are related to the Fermi level, which was also analyzed by neutral AuPd nanoparticle calculations. These charged calculations were performed with a uniform compensating background charge, and dipole-corrected energies were used to calculate these values.

The 201-atom nanoparticle contains 12 symmetrically unique locations for atoms: six on the surface (Figure 1a) and six in the subsurface (Figure 1b). These atoms vary in coordination number (CN) from 6 (corner atoms) to 12 (subsurface atoms). There are two unique edge sites (CN = 7): one at the intersection of two (111) terraces, which we denote “edge11,” and one at the edge joining a (111) terrace and a (100) terrace, which we denote “edge10.” All subsurface sites are labeled “sub” with a number that indicates how close the site is to the surface and a letter that indicates the proximity of that site (among those of its type) to a corner atom. For example, “sub2a” is two atoms away from the nearest surface atom and is the closest sub2 atom to a corner atom. There are two unique sites on the (111) facet: six that are adjacent to a corner atom (“t111a”) and one in the center of the (111) facet (“t111b”).

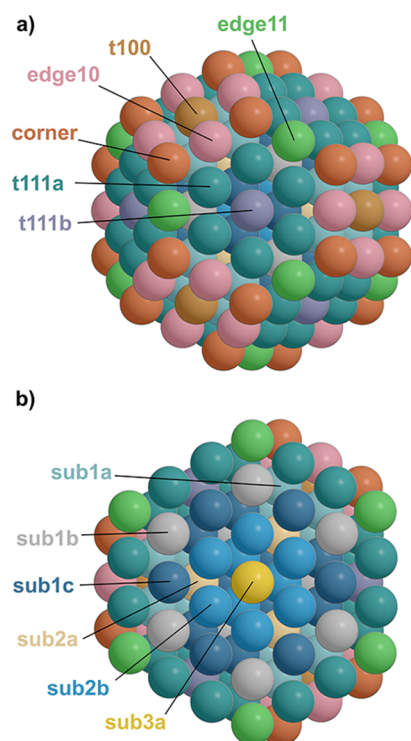
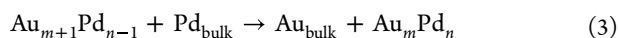


Figure 1. Ideal 201-atom nanoparticle models of (a) the full particle showing the six unique surface exchange sites: t111b (purple), t111a (blue-green), t100 (brown), edge10 (pink), edge11 (green), and corner (orange) and (b) the half particle showing the six unique subsurface sites: sub1a (sky blue), sub1b (gray), sub1c (dark blue), sub2a (beige), sub2b (light blue), and sub3a (gold).

DFT calculations were used to calculate the potential energies (E_0) of each nanoparticle and exchange energies (E_{ex}) required to replace an Au atom within a particle with a Pd atom using atoms from the respective bulk structures:



$$E_{\text{ex}} = E_{\text{Au}_m\text{Pd}_n} + E_{\text{Au,bulk}} - E_{\text{Pd,bulk}} - E_{\text{Au}_{m+1}\text{Pd}_{n-1}} \quad (4)$$

where $\text{Au}_{m+1}\text{Pd}_{n-1}$ is the structure before $\text{Au} \rightarrow \text{Pd}$ exchange and Au_mPd_n is the structure after. The difference between the two exchange energies, as described below, gives the energy to swap Pd atoms within AuPd nanoparticles (E_{swap} , useful for canonical MC simulations where the composition is held constant). Exchange energies were calculated at infinite Pd dilution ($E_{\text{ex},0}$, one Pd atom in the Au structure) for each of the 12 crystallographically distinct sites in Au_{201} and within the Au(111) and Au(100) slabs (considering only unconstrained atoms for the slabs). Furthermore, exchange energies (at each site) were calculated while varying the composition of the first coordination shell around the exchange site, the second coordination shell, and the overall composition of the alloy. The impacts of these features are described in subsequent sections.

2.2. Exchange Energy Models. Using these DFT data, we present two models for estimating exchange energies. The coordination shell model (CS-based) modifies the infinite-dilution exchange energies ($E_{\text{ex},0}$) based on the number of Pd atoms in the first (N_{CS1}) and second (N_{CS2}) coordination shell (Figure 2):

$$E_{\text{ex,est}} = E_{\text{ex},0} + N_{\text{CS1}}\epsilon_{\text{CS1}} + N_{\text{CS2}}\epsilon_{\text{CS2}} + \Delta E_{\text{Fermi}}\epsilon_f \quad (5)$$

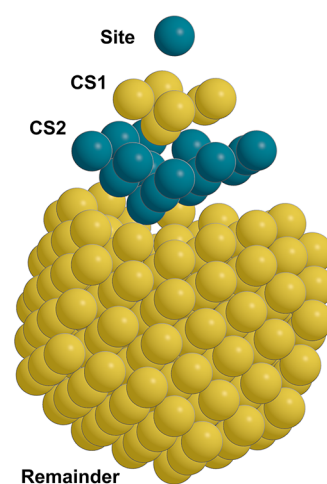


Figure 2. Particle model showing the first and second coordination shells for the corner exchange site.

where ϵ_{CS_x} (kJ mol^{-1}) are the energy penalties of Pd atoms in the first ($x = 1$) or second ($x = 2$) coordination shell around the exchange site, ΔE_{Fermi} is the difference between the Fermi level for a pure Au nanoparticle and the estimated Fermi level of the nanoparticle before exchange, and ϵ_f is the energy contribution of that Fermi level shift. These Fermi levels were averaged across a large set of representative structures across all possible compositions for the 201-atom nanoparticles and are tabulated in the [Supporting Information](#); thus, the Fermi levels used here are independent of the arrangement of Au and Pd atoms within the nanoparticle. Note, unlike models with more parameters (discussed below), the ϵ_{CS_x} penalties do not consider the location of atoms in their respective coordination shells, and the same ϵ_{CS_x} penalties are applied regardless of the exchange site. This model has a total of 15 parameters for describing exchange energies in a 201-atom nanoparticle (12 DFT-calculated $E_{\text{ex},0}$ values and 3 regressed ϵ values). Later, we will show that Pd atoms in the second coordination shell impact exchange energies, but atoms in the second coordination shell (unlike those in the first) are present at varying distances from the exchange site: distances of $2a$, $\sqrt{2}a$, and $\sqrt{3}a$, where a is an M–M bond distance. Thus, a modification of eq 5 was also considered:

$$E_{\text{ex,est}} = E_{\text{ex},0} + N_{\text{CS1}}\epsilon_{\text{CS1}} + \sum n_{D_i}\epsilon_{D_i} + \Delta E_{\text{Fermi}}\epsilon_f \quad (6)$$

where the $\sum n_{D_i}\epsilon_{D_i}$ represents terms accounting for the number of Pd at the three distinct positions in the second coordination shell (distances of $2a$, $\sqrt{2}a$, and $\sqrt{3}a$).

A model developed in prior work⁵⁴ used bond energies to describe the energies of AuPd surface alloys:

$$E_0 = \sum n_M\epsilon_M + \sum n_{M_i-N_j}\epsilon_{M_i-N_j} \quad (7)$$

where n_M is the number of metal atoms ($M = \text{Au, Pd}$), ϵ_M is the energy (per atom) of the bulk structures (calculated from DFT in this work as $\epsilon_{\text{Au}} = -2.6$ eV, $\epsilon_{\text{Pd}} = -4.6$ eV), $n_{M_i-N_j}$ and $\epsilon_{M_i-N_j}$ are the number and energies for each possible bond type, taking into account both the composition (M and N) of the bond and the locations (sites, i and j) of the two atoms within the structure. For example, for AuPd surface alloys, you could have Au–Au bonds between two surface Au atoms, between two subsurface Au atoms, or between surface and

subsurface Au atoms (with similar possibilities for Au–Pd and Pd–Pd bonds). For a AuPd alloy where Pd atoms are restricted to the first two layers of a AuPd (111) surface, as studied in previous work,⁵⁴ there would be 10 regressed parameters. For a 201-atom nanoparticle with six distinct site types (i.e., grouping the two (111) terrace sites and the six subsurface sites), there would be 2 parameters (ϵ_{Au} and ϵ_{Pd}) calculated by DFT and 50 $\epsilon_{M_i-N_j}$ parameters. Among these parameters, not all are independent of one another, so the $\epsilon_{\text{Au}_{\text{sub}}-\text{Au}_{\text{sub}}}$ and $\epsilon_{\text{Pd}_{\text{sub}}-\text{Pd}_{\text{sub}}}$ parameters are set to 0 such that eq 7 (along with the definitions of ϵ_M) perfectly recreates the DFT-calculated energies of bulk Au and bulk Pd. All other $\epsilon_{M_i-N_j}$ parameters (48) would be regressed to fit DFT data. This model is functionally similar to a cluster expansion approach, in which the only clusters present are adjacent metal pairs. The model in eq 7 only predicts system energies, so to get exchange energies, eq 4 would still have to be used. A different model can be considered which directly predicts exchange energies, as this may result in better agreement with DFT-calculated energies through cancellation of errors:

$$E_{\text{ex}} = \sum n_{M_i-N_j} \Delta \epsilon_{M_i-N_j} \quad (8)$$

where $n_{M_i-N_j}$ is the number of bonds of a given type (Pd–Pd or Au–Pd) that are formed when a given Au atom is replaced with a Pd atom, and $\Delta \epsilon_{M_i-N_j}$ is representative of the change in energy resulting from the bonds broken from removing the Au atom and the bonds formed by adding the Pd atom. This model has 48 regressed parameters, but as described below, it fails to account for any influence in the particle composition beyond the first coordination shell. In other words, exchanging Au for Pd is expected to be independent of the composition of the second coordination shell or of the extended nanoparticle, which we show is not the case. To improve upon this model, we add two additional terms:

$$E_{\text{ex}} = \sum n_{M_i-N_j} \Delta \epsilon_{M_i-N_j} + N_{\text{CS2}} \epsilon_{\text{CS2}} + \Delta E_{\text{Fermi}} \epsilon_f \quad (9)$$

where the last two terms are the same as those shown in eq 5. We also consider a version where the influence of atoms in the second coordination shell is broken down based on distance:

$$E_{\text{ex}} = \sum n_{M_i-N_j} \Delta \epsilon_{M_i-N_j} + \sum n_{D_i} \epsilon_{D_i} + \Delta E_{\text{Fermi}} \epsilon_f \quad (10)$$

where the last two terms are the same as those shown in eq 6.

2.3. Monte Carlo Simulations. Here, we performed canonical MC simulations to predict the structure of AuPd nanoparticles under a vacuum. MC simulations were started by using a pure Au nanoparticle, with Pd then added at random locations until the desired Pd content is met (as specified by the user). After this initial structure is made, two distinct atoms are randomly selected to be swapped; they do not have to be neighboring atoms. The probability (P) for this swap to occur is

$$P = \frac{1}{1 + e^{\Delta E_{\text{swap}}/kT}} \quad (11)$$

where the swap energy (ΔE_{swap}) is the difference between the Au-to-Pd exchange energies at the respective sites:

$$\Delta E_{\text{swap}} = E_{\text{ex},1} - E_{\text{ex},2} \quad (12)$$

If Site 1 was initially Au, a random number is then generated (between 0 and 1) and compared to the calculated probability (P , eq 11); if the random number is lower, then the swap occurs. This process is repeated until a maximum number of swaps (typically 2×10^4) or a maximum number of swap attempts (typically 2×10^6) were reached. After the MC simulation, several particle properties (e.g., average CN) are checked to make sure the particle structure had reached equilibrium (Figure 3). Given the stochastic nature of MC

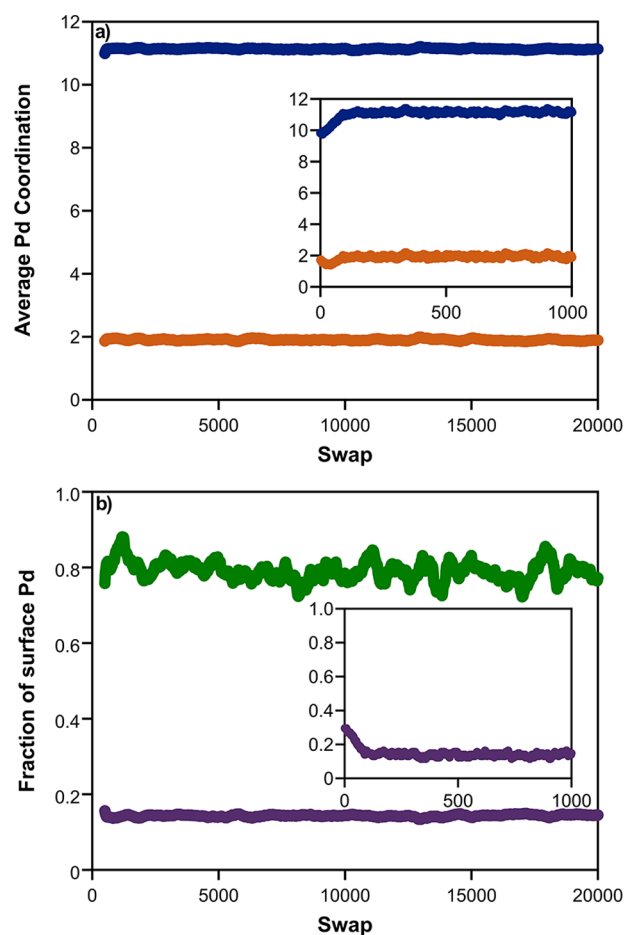


Figure 3. Plots of (a) the average coordination number for Pd atoms (blue) and the average number of Pd–Pd bonds (orange) and (b) the fraction of the surface that is Pd (purple) and the fraction of that surface Pd that is monomeric (green) for a simulation at 298 K and Pd mole fraction of 0.34. Plots show a rolling average of the last 500 structures. Insets show the transient region (first 1000 swaps) for these properties.

simulations, we report structural properties based on the average of the last 500 structures of a simulation; changing the size of this averaging window did not influence results because this averaging occurs well after equilibration of the nanoparticle structure. Given the random initiation of the particles during MC simulations, each MC simulation is repeated 20 times, resulting in a total of 10^5 averaged structures for all of the data reported below.

3. RESULTS AND DISCUSSION

Here, we use ideal particle models (without kinks, step-edges, or adatoms) to systematically probe the effects of exchange site, exchange environment, and overall composition on

exchange energies in AuPd nanoparticle alloys, with comparisons to surface alloys. As mentioned in Section 2, the truncated octahedral particles we focus on here are composed of eight hexagonal (111) terraces and six square (100) terraces connected by edge and corner atoms.

3.1. How Exchange Energies Are Impacted by Exchange Site. Exchange energies for the addition of a single Pd atom into a pure Au particle indicate that Pd prefers to be in the subsurface of the particle, as expected from prior studies.^{53,54,56–66,69} Exchange energies (eqs 3–4) at infinite Pd dilution ($E_{\text{ex},0}$) are calculated here at each of the 12 unique exchange sites (Figure 4); they decrease (become more

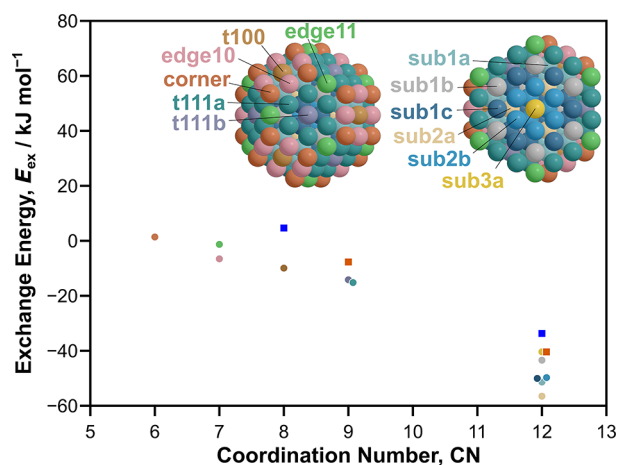


Figure 4. Exchange energies for adding a single Pd to a pure Au material versus the coordination number of the exchange site for a (111) slab model (orange squares), (100) slab model (blue squares), and each unique site in the 201-atom particle model: t111b (purple), t111a (blue-green), t100 (brown), edge10 (pink), edge11 (green), corner (orange), sub1a (sky blue), sub1b (gray), sub1c (dark blue), sub2a (beige), sub2b (light blue), and sub3a (gold).

exothermic) as the coordination number (CN) of the exchange site increases from 6 (corner site, $E_{\text{ex},0} = 1 \text{ kJ mol}^{-1}$) to 12 (subsurface sites, $E_{\text{ex},0} = -40$ to -57 kJ mol^{-1}). This decrease in $E_{\text{ex},0}$ is nearly linear with increasing CN, but it is notable that there is a significant variation in $E_{\text{ex},0}$ values across the six unique subsurface exchange sites in the 201-atom nanoparticle. Among exchange energies into subsurface sites, we examined three features to identify possible correlations: 1) the number of atoms in next-nearest-neighbor positions, 2) the average M–M bond distances before exchange, and 3) the distance from the exchange site to the center of the nanoparticle. Among these, none could account for variations in the exchange energies across the distinct subsurface sites, as shown in Figure S3.

We also calculated exchange energies for the two distinct sites in the top two layers of an Au(100) surface model (representing surface [CN = 8] and subsurface [CN = 12] sites) and in an Au(111) surface model (CN = 9 in surface and CN = 12 in subsurface). These data are 10–15 kJ mol^{-1} more endothermic than similar exchanges in their nanoparticle counterparts, likely because the Pd-doped Au nanoparticles can structurally relax more than Pd-doped surfaces, as the latter have constrained (i.e., frozen) atoms in the bottom two layers of the slab and have fixed unit cell parameters, while the nanoparticle is completely unconstrained and surrounded by a vacuum region in which it can contract or expand without

altering the unit cell parameters or interacting with nanoparticles in neighboring unit cells.

To test how sensitive exchange energies (and relative exchange energies) are to the choice of exchange-correlation functional, the calculations on the Au(111) surface were also performed using PBE, PBE-D3BJ, PBEsol, RPBE-D3BJ, optB880vdW, optB86b-vdW, and vdW-DF2. The exchange energies for these different functionals range from -8 to 15 kJ mol^{-1} for the surface site and -40 to -9 kJ mol^{-1} for the subsurface site (Figure S4). These data suggest that there is a significant variation in the formation energies of AuPd alloys (using bulk Au and Pd structures as reservoirs) across different GGA exchange-correlation functionals. This variation can also be seen in the formation energies of bulk AuPd alloys:

$$E_{\text{ex,bulk}} = E_{\text{Au}_3\text{Pd}_1,\text{bulk}} - E_{\text{Au,bulk}} - E_{\text{Pd,bulk}} \quad (13)$$

which vary from -40 to 9 kJ mol^{-1} across the GGA functionals listed, matching the variation for exchange into subsurface sites in Au(111) models. However, the differences between the exchange energies (i.e., the swap energies) for each functional vary much less than the individual exchange energies. Surface-to-subsurface swap energies range from -36 to -24 kJ mol^{-1} across the functionals studied here. Furthermore, two functionals (RPBE-D3BJ, vdW-DF2) appear to be outliers in these swap energy calculations, as most vary from -36 to -32 kJ mol^{-1} . As we are using these DFT-based models to predict swap energies in the context of canonical MC simulations, this relatively low variation in swap energies suggests that our choice of functionals would not significantly impact our structural predictions for these AuPd materials.

Overall, these dilute exchange energies ($E_{\text{ex},0}$) indicate that Pd prefers to be in the subsurface of the nanoparticle, matching the conclusions of prior^{53,54,56–58,60–66,69} studies of AuPd alloys. Furthermore, it suggests that Pd exchange becomes more difficult as the CN of the exchange site decreases, such that Pd atoms are more likely to occupy high-CN surface sites (e.g., in the (111) terrace) than low-CN sites (e.g., at nanoparticle corners). Among subsurface sites, there is significant variation (up to 20 kJ mol^{-1}) in exchange energies, but we have been unable to rationalize those differences.

3.2. Effects of Pd in First and Second Coordination Shells. Exchange energies become more unfavorable with an increasing number of Pd neighbors in the first coordination shell around the exchange site, with relatively minor variation caused by the location of the Pd atoms within the shell. Calculations were performed for exchange into sites with varying amounts of Pd in the first coordination shell, up to a shell full of Pd. For the corner site (CN = 6), all 35 unique configurations of Pd atoms within the six-atom coordination shell (1 for Au_6 , 4 for Au_5Pd_1 , 8 for Au_4Pd_2 , 9 for Au_3Pd_3 , 8 for Au_2Pd_4 , 4 for Au_1Pd_5 , and 1 for Pd_6) were modeled. Exchange energies increase linearly from 1 kJ mol^{-1} to 60 kJ mol^{-1} as the number of Pd in the first coordination shell increased from 0 to 6. When a single Pd atom is in the coordination shell, there are four different unique positions in which it can reside, and the exchange energies vary from 10 to 13 kJ mol^{-1} . This small range in energies with varying Pd positions in the first coordination shell and similar trends for the 8 Au_4Pd_2 configurations (and others) indicate that there is a relatively weak influence on the position of Pd in the first coordination shell. For the remaining exchange sites, rather than considering all possible Pd arrangements in their coordination shells, 4–5 (in most cases) random configurations were used for each

number of Pd atoms in the coordination shell. The scatter in exchange energies among configurations (of a given composition) remains small ($<10 \text{ kJ mol}^{-1}$), suggesting that the location of Pd within the first coordination shell is less important than the amount of Pd in determining the exchange energy (Figure 5). Exchange energies, across all sites, increase

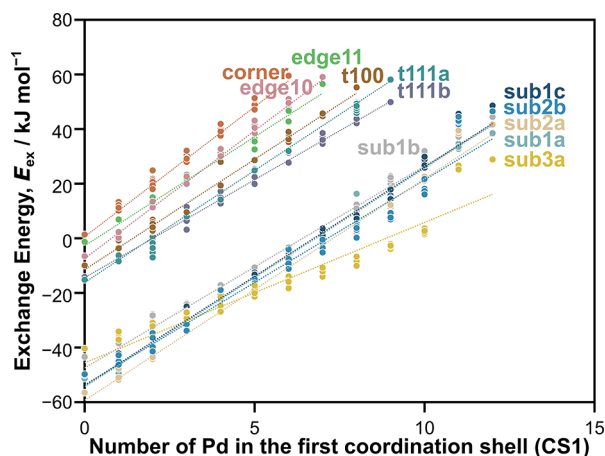


Figure 5. Exchange energies vs the number of Pd in the first coordination shell for each unique exchange site in the 201-atom particle model: t111b (purple), t111a (blue-green), t100 (brown), edge10 (pink), edge11 (green), corner (orange), sub1a (sky blue), sub1b (gray), sub1c (dark blue), sub2a (beige), sub2b (light blue), and sub3a (gold). Figure S5 shows these data in 12 individual plots to improve readability.

linearly with the number of Pd atoms in the first coordination shell, indicating that Pd prefers to be isolated from one another. These results agree with previous computational studies on slab and particle models of AuPd alloys.^{53,54,61,62,70} CO-DRIFTS and IRAS studies both confirmed through the absence of peaks associated with Pd clusters that Pd prefers to be isolated within Au.^{53,55}

The slopes in Figure 5 represent the penalties associated with forming Pd–Pd bonds rather than Pd–Au bonds, and they are nearly identical, ranging from 7.2 to $9.5 \text{ kJ mol}^{-1} \text{ Pd}^{-1}$ for most sites. Exchange into the “sub3a” site, however, is an outlier; for that site, the exchange energy increases from -40 to 4 kJ mol^{-1} as the number of Pd neighbors increases from 0 to 10 (slope: $4.1 \text{ mol}^{-1} \text{ Pd}^{-1}$ in this range), and then the exchange energy jumps to 25 kJ mol^{-1} for 11 neighbors and 29 kJ mol^{-1} for 12 neighbors. Similar breaks between 10 and 11 Pd neighbors are present for exchanges into other subsurface sites (see Figure S5 for exchange energy plots separated by site type), although the break is most noticeable in the sub3a data set. The break in linearity was also observed in a previous study of 201-atom AuPd nanoparticles,⁷¹ which noted that the energies of nanoparticles jumped in energy comparing $\text{Au}_{190}\text{Pd}_{11}$ and $\text{Au}_{191}\text{Pd}_{10}$ compositions, regardless of Pd arrangement. This break in linearity is related to a sudden change in the electronic properties of the nanoparticle at that composition, as described in Section 3.3. Given our focus here on SAA catalysts, and thus on materials with high (>20) Au:Pd ratios, it is unlikely that exchange energies into subsurface sites with 11 or 12 neighbors will be relevant (many compositions of interest will not have that many Pd atoms in total, much less in high proximity given that Pd usually remains dispersed). Focusing on ≤ 10 Pd neighbors in CS1, all data show good

agreement with a linear fit, with an average slope (weighted based on the number of atoms of each site type) of $8.1 \text{ kJ mol}^{-1} \text{ Pd}^{-1}$. This value is the ϵ_{CS1} parameter in eqs 5 and 6, which can also be linearly regressed to a broader set of DFT training data, as described later.

These exchange energies at different sites and with different numbers of Pd in neighboring positions suggest that as Pd content in an Au nanoparticle increases, it will first occupy isolated subsurface sites, followed by subsurface sites with few (≤ 5 neighbors). However, exchange into subsurface sites with >5 neighbors has similar exchange energies to high-CN surface sites (e.g., sites in the (111) terrace), suggesting Pd atoms will appear on the surface once subsurface sites become crowded. In other words, the penalty ($\epsilon_{\text{CS1}} = 8.1 \text{ kJ mol}^{-1}$) associated with forming Pd–Pd bonds would prevent the formation of a core–shell structure, which would be much more likely to occur if ϵ_{CS1} was instead near 0 or negative.

Exchanging Pd into the particle is less favorable for sites with more Pd in their second coordination shell but to a lesser degree than the impacts of Pd in the first coordination shell. The size of the second coordination shell ranges from 16 atoms (corner, CN = 6) to 42 atoms (sub2 and sub3, CN = 12). Similar to Figure 5, exchange energies were calculated as a function of Pd content in the second coordination shell for all primary exchange sites; five random configurations of Pd in CS2 were made for each Pd content (Figure 6). Because we

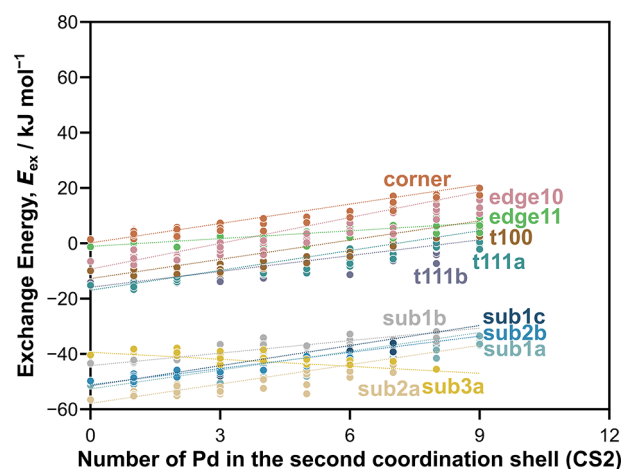


Figure 6. Exchange energies vs the number of Pd in the second coordination shell for each unique exchange site in the 201-atom particle model: t111b (purple), t111a (blue-green), t100 (brown), edge10 (pink), edge11 (green), corner (orange), sub1a (sky blue), sub1b (gray), sub1c (dark blue), sub2a (beige), sub2b (light blue), and sub3a (gold).

are primarily interested in dilute materials, we focused on compositions of up to 9 Pd atoms in the second coordination shell. Pd atoms in the second coordination shell around an exchange site increase exchange energies (similar to impacts in CS1, Figure 5). However, the slopes (-0.7 to $2.5 \text{ kJ mol}^{-1} \text{ Pd}^{-1}$) are much smaller, suggesting that Pd in CS2 has much less of an effect on exchange energies than Pd in CS1, as expected. Also, like in Figure 5, exchange into the sub3a site also follows a different trend, with exchange energies becoming slightly more exothermic as the number of Pd in CS2 increases. Overall, the weighted average of the impact of Pd in the second coordination shell (ϵ_{CS2} , slopes in Figure 6) is $1.8 \text{ kJ mol}^{-1} \text{ Pd}^{-1}$.

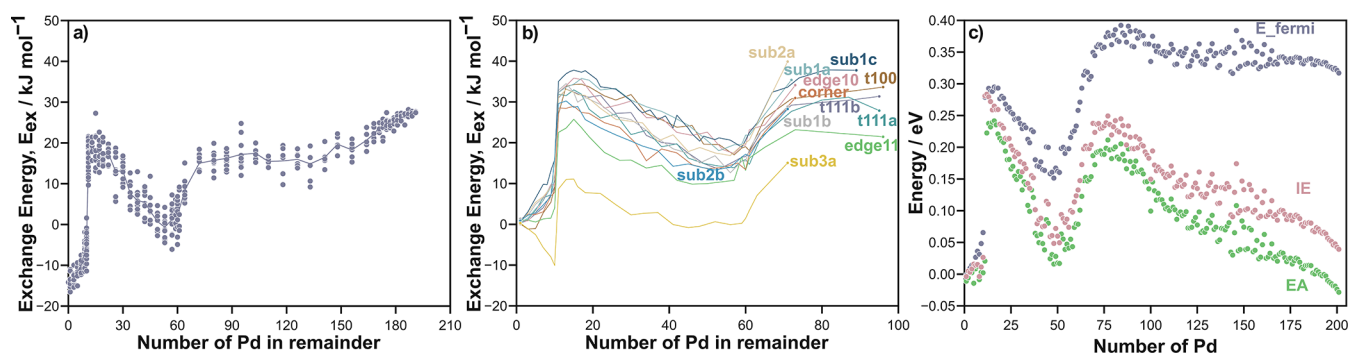


Figure 7. Plot for exchange energies versus the number of Pd in the remainder of the particle for (a) the t111b exchange site in the 201-atom particle model and (b) other exchange sites: t111b (purple), t111a (blue-green), t100 (brown), edge10 (pink), edge11 (green), corner (orange), sub1a (sky blue), sub1b (gray), sub1c (dark blue), sub2a (beige), sub2b (light blue), and sub3a (gold). For simplicity, all data points are shown in part (a), along with a moving average line, while in part (b), only the moving average lines are shown. Versions with all data points are shown for each exchange site in Figure S7. Plot of (c) Fermi energy (purple), ionization energy (pink), and electron affinity (green) versus the number of Pd in the extended nanoparticle.

3.3. Effects of Pd in the Extended Nanoparticle.

Exchange energies for substituting Pd into Au sites in AuPd nanoparticles were also calculated as a function of the overall Pd composition. Exchange energies were calculated for the 12 exchange sites with varying Pd contents in the extended nanoparticle region (i.e., the region outside of the first coordination shell). The first coordination shell was kept fixed as pure Au. The arrangement of atoms in the extended nanoparticle region was random, with 5–10 configurations (for some, 30 configurations were calculated) for each composition. A nonlinear trend is observed for exchange energies as the Pd content in this region increases. Exchange into a t111b site, for example, increases from -15 kJ mol^{-1} to -5 kJ mol^{-1} up to 10 Pd atoms, then jumps to $+15 \text{ kJ mol}^{-1}$ for 11 Pd atoms. The E_{ex} values gradually decrease to near 0 kJ mol^{-1} for 59 Pd atoms in the “remainder” region and then increase again to values near $+10 \text{ kJ mol}^{-1}$ for 75 atoms, followed by a relatively monotonic increase in E_{ex} to a value near 28 kJ mol^{-1} when the remainder region is 100% Pd (going from $\text{Au}_{10}\text{Pd}_{191}$ to $\text{Au}_0\text{Pd}_{192}$, as the first coordination shell is maintained as pure Au). Similar increases in exchange energies are seen in Figures 5 and 7b for exchange into structures with 11 Pd atoms (to make $\text{Au}_{189}\text{Pd}_{12}$). In the context of a canonical MC simulation, where swap energies are of interest and the nanoparticle composition is held fixed, many of these variations with the composition in the extended nanoparticle region will cancel out. Indeed, the curves in Figure 7b are nearly parallel, indicating that swapping Pd atoms between these positions will be nearly constant within the scatter expected from these data. That said, these exchange energies would impact grand canonical MC simulations where nanoparticle composition is predicted alongside structure, and thus, some investigation into this nonmonotonic behavior is warranted.

These ubiquitous jumps in exchange energy suggest that the electronic energy itself changes abruptly as the number of Pd atoms in the 201-atom nanoparticle increases from 11 to 12. This abrupt change has been recognized in a previous study of AuPd 201-atom nanoparticles⁷¹ and is related to the electronic energy levels present within a Au 201-atom nanoparticle. Replacing Au with Pd reduces the number of valence electrons in the 201-atom nanoparticle by 1, and thus, examining the highest filled electronic energy levels in a Au_{201} nanoparticle will give some insights into the energy of AuPd alloys. As discussed further in Section S2.3, the 6 highest energy levels

(corresponding to 11 electrons as one is half-filled) have energies near -2.0 eV , while the seventh-highest energy level has an energy near -2.4 eV . In other words, an abrupt energy change is expected as the number of Pd atoms goes from 11 to 12. A similarly abrupt change in energy levels (of 0.4 eV) occurs between the 32nd and 33rd highest energy levels, corresponding to a Pd composition near 60, which is close to another sudden change in exchange energies as shown in Figures 7 and S7. Energy levels for remaining states change gradually (no changes $>0.05 \text{ eV}$) for those occupied by the 201 highest energy electrons (exchanging every Au for Pd in a 201-atom nanoparticle), indicating that no other abrupt changes in exchange energies would be expected based on these electronic states. These energy levels would also predict an abrupt change in the electronic energies of cationic Au_{201} nanoparticles because Au_{201}^{n+} has the same number of electrons as $\text{Au}_{201-n}\text{Pd}_n$. Indeed, Figure S9 shows that the second derivative of the electronic energy $\left(\frac{\partial^2 E_0}{\partial z^2}\right)$ is $\sim 0.4 \text{ eV}$ higher for a charge of 11 ($z = 11$) as the charge is varied from 0 to 30, which is the same as the change in the energy levels obtained from the Au_{201} (neutral) calculation.

While these changes in band energies are informative, they are not numerically predictive because energy levels will also change with composition. As the number of Pd increases, the energy levels described above will shift (both because electrons are being removed and because the composition is changing). We can also see changes in the electronic structure of these nanoparticles by examining the DFT-calculated Fermi levels. However, Fermi levels will depend on both the arrangement and composition of the nanoparticle, and here, we are only interested in long-range effects caused by changes in composition. Therefore, we took a set of three MC-generated structures for AuPd alloys of all possible compositions (1000 total structures). For those structures, we optimized them and calculated their Fermi levels. Furthermore, we calculated the energies of their charged anionic and cationic forms to calculate their electron affinities and ionization energies. The results, shown in Figure 7c, are plotted as a function of the change in these properties (E_{Fermi} , EA, IE) with respect to the pure Au nanoparticle; for E_{Fermi} and EA, we multiplied these values by -1 because $\text{Au} \rightarrow \text{Pd}$ exchange removes an electron, rather than adding one. These electronic properties vary with nanoparticle composition, similar to the manner in which the

exchange energies vary (Figure 7a,b). Among these, ΔE_{Fermi} bears the most resemblance, as EA and IE show a monotonic decrease in magnitude as the Pd content increases from 80 to 200 atoms, while the Fermi level remains mostly constant (while the exchange energies in Figure 7a slightly increase). As described in Section 2, these Fermi levels are used in models to improve exchange energy predictions.

3.4. Modeling Exchange Energies. Prior studies have developed models (based on bonding⁵⁴ or using cluster expansion^{52,70–73} or neural network⁶⁹ approaches) to predict electronic energies of alloy structures. Here, we evaluate a bond-energy model, adapted from Tysoe and coworkers,⁵⁴ but we first examined a simpler model. As described above, exchange energies linearly increased with the number of Pd atoms in the first coordination shell and were weakly impacted by Pd in the second coordination shell. As such, we first evaluated a simple model to predict exchange energies as perturbations to infinite-dilution exchange energies ($E_{\text{ex},0}$) informed by the number of Pd in each coordination shell, and the change in the Fermi level caused by changes in composition (eq 5). These three terms are roughly included to account for changes in exchange energy described in Figures 5, 6, and 7. The model was regressed to those data, and when fit to the training set, ϵ_{CS1} is 6.1 and ϵ_{CS2} is 0.1 $\text{kJ mol}^{-1} \text{Pd}^{-1}$, consistent with the smaller impacts of Pd in the second coordination shell (Figure 6), and ϵ_f is -0.93 . We also evaluated a second version of this model, where atoms in the second coordination shell are separated into 3 groups based on the atoms' distance from the exchange sites (eq 6), but this variation of the model did not reduce the model's error; as such, that version of the model was discarded. The CS-based model (with 3 regressed parameters) shows reasonable parity with the DFT calculated exchange energies (Figure 8a) with a median absolute error (MAE) of 3.9 kJ mol^{-1} and a root-mean-squared error (RMSE) of 7.0 kJ mol^{-1} .

As discussed in Section 2, we adapted a physical model from Tysoe and coworkers,⁵⁴ based on variations in bond energies between Au–Au, Au–Pd, and Pd–Pd bonds (and variations in bond energies between atoms in different environments). This model had previously been used to predict the energies of AuPd(111) surfaces. We evaluated this model to predict energies of AuPd nanoparticles directly, but changes in the electronic structure described in Section 3.3 prevented high-quality predictions. In prior work using a cluster expansion model to predict AuPd nanoparticle energies,⁷¹ these same electronic structure variations led them to regress parameters, independently, for every composition of interest, resulting in a very large number of regressed parameters ($>10^3$) and an increased need for training data. Given our main interest in using this model to inform canonical MC simulations at high Au/Pd ratios, it seems unnecessary to fit system energies instead of directly regressing exchange energies. This is convenient given that our DFT data are already structured to calculate exchange energies (Figures 4–7), and one would expect some beneficial cancellation of errors, leading to greater accuracy. Canonical MC simulations require swap energies, not exchange energies, but we have relatively few swap energies calculated for this work, and exchange energies can always be used to calculate swap energies for canonical MC simulations, or they can be used directly in grand canonical MC simulations. We fit this model, first just to the data for exchanges at infinite dilution and with Pd in the first coordination shell (Figure S13). This fit can reasonably

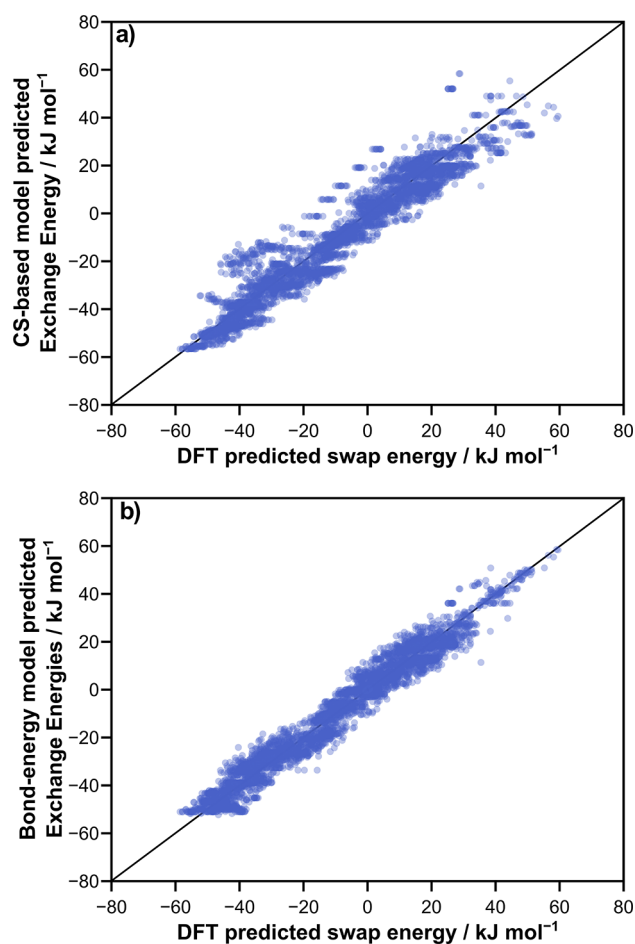


Figure 8. Plots showing parity between (a) exchange energy predicted with the CS-based model and (b) bond-energy model versus DFT-calculated exchange energy. Points are made partly transparent, so that the “density” of data points is observable.

predict swap energies through a cancellation of errors but is not able to capture the changes in the electronic structure previously discussed. Therefore, we also expanded the model to add contribution terms related to Pd atoms in the second coordination shell and related to the Fermi level of the nanoparticle before exchange (these terms are the same as those described above for the simple model), and as was the case for the simple model, the inclusion of the second coordination shell using 3 distinct parameters (eq 10) versus 1 parameter (eq 9) led to negligible improvement of the model. So, like for the CS-based model, the 1-parameter version of the model was chosen for simplicity.

This bond-energy model provides more accuracy than the CS-based models, though it is more complex. As described in Section 2, this model has 48 regressed parameters, compared to 3 for the CS model discussed above. The bond-energy model shows better parity with DFT than the CS model (Figure 9b), with an MAE of 3.4 kJ mol^{-1} and a RMSE of 5.0 kJ mol^{-1} or approximately 30% better than that of the CS-based model (12 calculated and 3 regressed parameters). The ϵ_{CS2} is 0.1 $\text{kJ mol}^{-1} \text{Pd}^{-1}$ and ϵ_f is -0.86 , and these values are similar to those regressed in the simpler CS-based model. The parity plot shows significantly less scatter (contrasting Figure 8a,b), and the residuals (error) between the DFT-calculated and model-predicted exchange energies show essentially no bias with Pd content, unlike the CS-based model, which

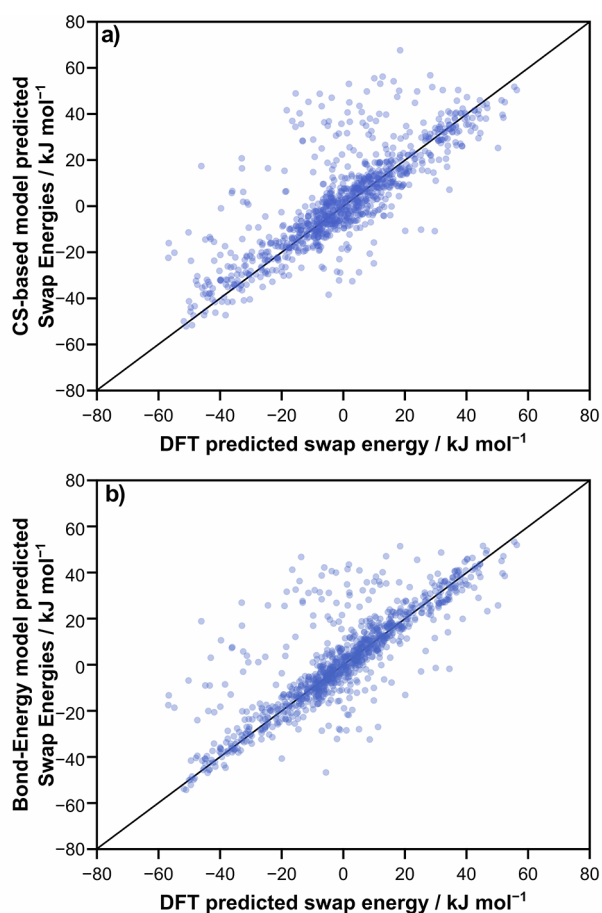


Figure 9. Parity plots for the (a) CS-based model and (b) bond-energy-model-predicted swap energies versus the DFT-calculated swap energies. Points are made partly transparent, so that the “density” of data points is observable.

performs better at low Pd compositions. Overall, the bond-energy model is better able to predict exchange energies than the CS-based models but with many more parameters than the CS-based model.

These models, however, were informed by many DFT-calculated exchange energies that were set up to answer specific questions without regard to the likelihood of those scenarios. For example, Pd exchanging into a site with 12 Pd neighbors to form an $\text{Au}_{188}\text{Pd}_{13}$ nanoparticle with minimal Pd dispersion is a very unlikely scenario, as our data shows Pd wants to spread out within the nanoparticle to minimize Pd–Pd bonds. To assess their performance in MC simulations, we used MC simulations to predict 1000 $\text{Au}_{125}\text{Pd}_{76}$ structures during equilibrium and optimized them by using DFT to compute their swap energies. Figure 9 shows that there is more scatter in these swap energy predictions than in the exchange energy predictions, which is somewhat expected given that the models were fit to exchange energies and not to swap energies. Differences in scatter show that the 3-parameter CS-based model is significantly worse than the 50-parameter bond-energy model and to a larger extent than differences in parity within exchange energy predictions. The CS-based model, furthermore, appears to consistently underpredict swaps that are unfavorable ($\Delta E_{\text{swap}} > 0$) and consistently overpredict swaps that are favorable ($\Delta E_{\text{swap}} < 0$). For both models, DFT data points often fall above the parity line, suggesting that model-predicted swap energies are more endothermic than

those calculated by DFT. Overall, the MAE values are 4.8 and 3.3 kJ mol^{-1} for the CS-comp and bond-energy models, respectively, while the RMSE values are 13.0 and 12.0 kJ mol^{-1} . These results suggest, as discussed above, that the bond-energy models would be preferred in MC simulations, while the simpler CS-comp models are useful in their simplicity and act as simple guides to understanding these nanoparticle structures.

3.5. Predicted Nanoparticle Structure Under Vacuum.

MC simulations were set up to predict the structure (arrangement of metal atoms) in 201-atom AuPd nanoparticles as a function of composition by using both the bond-energy and CS-based models. For each composition, 20 MC simulations were performed, and from each simulation, the 500 final structures were averaged together (and all 500 structures are after the system has equilibrated), so data below reflect an average of 10,000 equilibrium structures for each composition. We focus first on the results for the bond-energy model. Results suggest that Pd will fill the subsurface until a “breakthrough” is reached, where Pd starts to occupy surface sites. Essentially, all Pd atoms remain in the subsurface for Pd compositions up to 22 mol % or about 45 Pd (Figure 10a). As Pd content increases up to 22 mol %, the average Pd–Pd CN increases from 0 (indicating fully dispersed Pd) to values near 4. There are 79 subsurface atoms in the 201-atom model; therefore, Pd starts to populate the surface once half the subsurface sites are filled. For larger nanoparticles, where a higher fraction of metals is in the subsurface, one would expect this breakthrough composition to be larger. As shown in Figure 5, Pd prefers to exchange into subsurface sites unless those subsurface sites have many Pd neighbors, in which exchange into surface sites becomes more favorable. Pd exchange into surface sites is also driven by configurational entropy considerations, as (at this breakpoint composition) there are 122 surface sites and roughly 40 unoccupied subsurface sites. To form a core–shell alloy, in a vacuum, one would need a metal that 1) strongly prefers to be in the subsurface rather than at the surface and 2) prefers to bind to itself rather than the other metal in the alloy. Of course, given those requirements may be met, the alloy may not be miscible or easily formed at all, which is why surfactants are typically used to restructure alloys into core–shell arrangements during or after their synthesis. As the Pd content continues to increase, Pd starts to fill the surface and subsurface sites at roughly equal proportions, resulting in a decrease in Pd–M CN and a decrease in the slope of the Pd–Pd CN with composition (because Pd starts to occupy surface sites, it is easier to avoid other Pd atoms that are present in higher concentrations in the subsurface). Broadly, these trends are expected from prior work and the DFT data presented above; this validates that our MC simulation is generating reasonable data based on the DFT input and allows one to quantify certain features, such as surface ensembles that may be responsible for surface chemistry.

We divide Pd surface ensembles into 4 different ensemble types: monomers as any Pd isolated on the surface, dimers as any two neighboring atoms, trimers as any group of 3 atoms that form a triangle on the (111) terraces, and tetramers as any group of 4 atoms that form a square on the (100) terraces. These ensembles are identified here simply because they correspond to common binding modes (atop, bridge, 3-fold, and 4-fold) for species relevant to catalysis. Ensembles, as defined here, can partially overlap, meaning a dimer ensemble

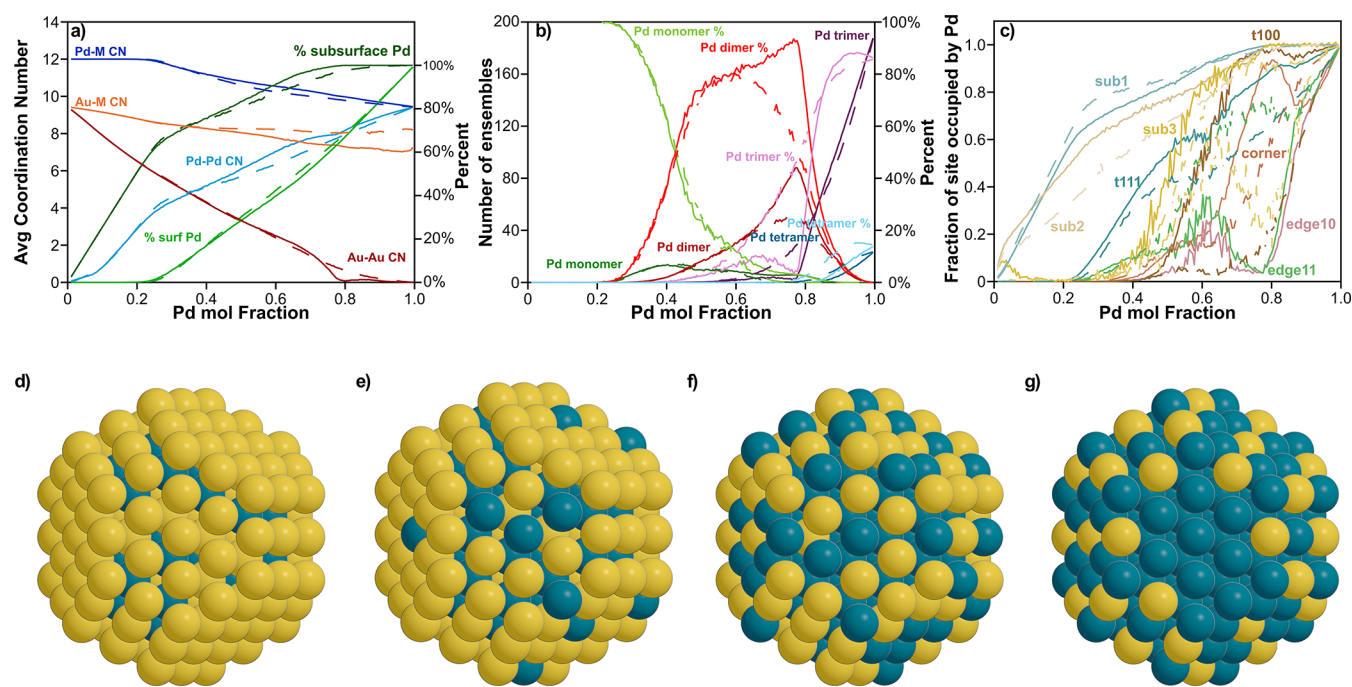


Figure 10. Plots of MC simulations using two different exchange energy models: the CS-comp. model (eq 5, 3 regressed parameters, dashed line) and the bond-energy model (eq 9, 48 regressed parameters, solid line). Particle structures under vacuum at 298 K are summarized showing (a) average number of bonds of Pd to other metal atoms (blue), average number of Pd–Pd bonds (light blue), average number of bonds of Au to other metal atoms (orange), average number of Au–Au bonds (dark red), percentage of surface that is Pd (light green) and percentage of subsurface that is Pd (dark green), (b) number of Pd monomers (green), Pd dimers (dark red), Pd trimers (purple), and tetramers (blue) in the surface and percentage of Pd monomers (light green), Pd dimers (red), Pd trimers (pink), and tetramers (light blue) in the surface versus mole fraction of Pd in the particle, and (c) the fraction of unique sites occupied by Pd versus the total number of Pd in the particle. Some lumping was done for (c): sub1 (green), sub2 (dark blue), and t111 (teal), each representing more than 1 of the 12 unique sites previously identified. The remaining sites are sub3 (brown), t100 (light blue), corner (orange), edge10 (gray), and edge11 (yellow). Also shown are structure images of the MC-predicted particle at (d) 44 Pd, (e) 78 Pd, (f) 120 Pd, and (g) 160 Pd.

can share one atom with a trimer, but both dimer atoms cannot be in the trimer ensemble. Pd is rarely at the surface at low (<20 mol %) compositions, but when present, it is present as a monomer. As soon as Pd starts to appreciably occupy surface sites (near 25 mol % Pd), the percentage of Pd_{surf} forming dimer ensembles increases along with a corresponding decrease in the percentage of Pd_{surf} in monomers (Figure 10b). This is a bit unexpected, given that Pd prefers to be isolated from itself. Obviously, as more Pd is added to the particle, isolated Pd will have to give way to Pd ensembles, but what is surprising is that Pd dimers do not significantly lag behind Pd monomers. By 30 mol % Pd, already ~10% of the surface Pd atoms are in Pd dimers. The number of monomers continues to increase until about 40 mol %, where a maximum of about 13 monomers is reached, far fewer than the 38 monomers that could be formed (without forming any Pd dimers) on this 201-atom nanoparticle (122 surface sites). However, that 38-monomer structure (Figure S11) would have a large number of Pd atoms at undercoordinated edge and corner sites, which Figure 5 shows us are relatively unstable compared to the higher-coordinated sites in the six (100) and eight (111) terraces. These terraces, however, can only fit 1–3 Pd atoms without forming dimers, resulting in a maximum of 30 Pd monomers if Pd only occupies those terrace sites, still far more than the maximum (13) reached by the MC simulations. This suggests that the penalty for forming Pd–Pd bonds is too low to reach higher monomer surface coverage given the configurational entropy effects driving dimer formation. Given the relationship between the size of these terraces and

the maximum number of Pd monomers one can form, it is clear that the compositions which maximize certain surface features will depend on particle size and morphology, as will be discussed in future work. If Pd monomers are the desired surface complex, these results would suggest that an Au/Pd ratio near 1.6 would be desired. However, for SAA applications, it is typically more important to minimize the number of Pd dimers and trimers than it is to maximize the number of Pd monomers, as dimers and trimers often present significant selectivity or stability challenges. In those cases, one would operate at Au/Pd ratios >5, as is typically the case, such that all Pd on the surface are monomeric.

At Pd compositions near 45 mol % Pd, Pd dimers become the most abundant surface ensemble, and some Pd trimers begin to form. At about 55 mol %, the percentage of Pd_{surf} present in dimers reaches a maximum of about 95%, and percentage of Pd_{surf} present in trimers surpasses that present as monomers. The number of Pd dimers goes through a maximum of ~62 dimers at 77 mol %. The surface becomes dominated by Pd trimers around 80 mol %. At about 85 mol %, the number and percentage of tetramers begin to increase, and the percentage of Pd_{surf} in trimers begins to plateau around 86–87%. Tetramers are the last ensembles to be populated here, in part because those ensembles consist of three undercoordinated edge and corner atoms given the small (100) terraces on this ~2 nm particle, and undercoordinated sites are the most inherently unstable exchange locations for Pd (Figures 4 and 5).

To get a more granular picture of where Pd atoms reside on the surface, Figure 10c shows the fraction of atoms of each site type that are Pd as the number of Pd atoms in the particle is increased from MC simulations. As expected, the subsurface sites are first populated, with sub1 and sub2 sites being filled with Pd, almost exclusively, until t111 sites start to populate at the breakthrough composition described above. The sub3 site (there is only one) is somewhat surprisingly mostly Au until compositions well above the breakthrough; this is likely because the sub3 site has 12 sub2 neighbors (and these are 60–70% Pd by the time Pd starts to populate surface sites); thus, to maximize the number of Pd atoms in the subsurface while minimizing the number of Pd–Pd bonds, the MC simulations find that the sub3 site remains as Au. Among surface sites, t111 sites fill first, reaching ~80% Pd before t100 sites become more favorable. This follows the trends expected in Figures 4 and 5 that sites populate in order of their CN, with t111 (CN = 9) coming before t100 (CN = 8). This trend with CN continues in Figure 4 through edge (CN = 7) and corner (CN = 6) atoms; however, the MC simulations show that corner sites tend to fill with Pd before edge sites. Corner sites would typically be the least favorable for exchange in dilute AuPd alloys given they have the lowest CN, but at this point, sub1, t111, and t100 sites are mostly full, and corner atoms have 3 neighbors of those types, while edge sites have 5 such neighbors. Once about 80% of the corner sites have been filled with Pd, the percentage plateaus, and edge sites start to become populated.

The MC results for the CS-based model show some key differences in comparison to those of the bond-energy model, but many of the trends are the same. Trends in Pd–M CN, Pd–Pd CN, Au–Au CN, the percentage of Pd at the surface, and the percentage of Pd in the subsurface are all almost identical between the two models. There is an observable deviation in the Au–M CN at Pd mole fractions >50% (Figure 10a). This difference can be traced to the filling of the surface sites, as the edge sites (both edge10 and edge11) fill with Pd at lower total Pd contents (~50% Pd) than what was observed for the bond-energy model. Conversely, the t111 and t100 sites fill at higher Pd contents (t111 still starts filling around 20% Pd, but the slope decreases around 50% Pd; t100 sites become some of the last sites filled around 80% total Pd) than the bond-energy model, meaning that more Au atoms will be occupying t111 (CN = 9) and t100 (CN = 7) over edge sites (CN = 7), causing this deviation in Au–M CN (Figure 10c). Differences in the filling of subsurface sites are relatively minor, with sub1 filling being almost the same between the two models. The filling of sub2 sites occurs at slightly higher Pd contents for the CS-based model, but overall, sub2 sites are still significantly filled before any surface sites. The sub3 site does show a larger deviation, becoming one of the last sites filled with Pd (around 80% total Pd); however, because there is only 1 sub3 site, its effect on the total particle behavior is minimal. Finally, the corner sites start filling at about the same Pd content, but after about 60% total Pd, the CS-based model fills slightly “slower” than the bond-energy model.

The formation of Pd monomers, dimers, trimers, and tetramers matches pretty closely in behavior between the two models at lower Pd contents, most relevant to SAA materials, but starts to differ at high Pd contents. Both the numbers and percentages of monomers and dimers match very closely between the bond-energy and CS-based models at <60% Pd. However, between 60% and 80%, trimers start to form using

the CS-based model, leading to differences. These slight shifts in behavior demonstrate that the CS-based model, despite having far fewer (3) regressed parameters than the bond-energy model (48), still captures the expected structural evolution of AuPd nanoparticles with increasing Pd coverage.

An increase in temperature allows for more Pd to reach the surface because higher energy states become accessible at higher temperatures. The results from the bond-energy model MC for percentage of Pd_{surf} with varying temperatures (200–800 K) for 201-atom particles ranging from 5 to 25 mol % Pd show that with increasing temperature, there is an increasing amount of Pd at the surface, which becomes more pronounced with higher Pd contents (Figure 11). Following the Boltzmann

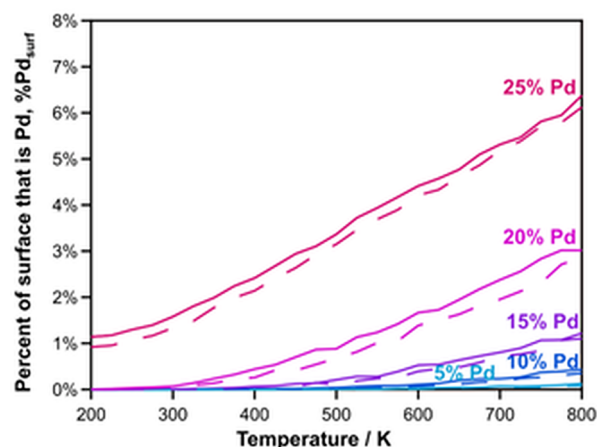


Figure 11. MC results for percentage of surface (Pd_{surf}) that is Pd versus temperature for 201-atom particles for varying Pd mol composition, 5% mol Pd (light blue), 10% mol Pd (dark blue), 15% mol Pd (purple), 20% mol Pd (pink), and 25% mol Pd (red). Results for the bond-energy model are shown as solid lines, and the results from the CS-comp model are shown as dashed lines.

distribution, a higher temperature favors states with higher energy, making such states more probable (eq 11). According to the Gibbs free energy equation, higher temperatures also make high entropy states more likely. Therefore, an increase in temperature allows certain barriers to be overcome, and Pd starts populating these higher energy states. For 5 mol % Pd, there is a very small change in the percentage of Pd_{surf} (~0–0.13 mol %) with increasing temperature. In the case of 10 mol %, 15 mol %, and 20 mol % Pd, the change of Pd_{surf} is from ~0% to 0.45%, 1.37%, and 3.22%, respectively. For 25 mol % Pd, there is a larger increase in the percentage of Pd_{surf} (1.51–6.42%), with increasing temperature. Overall, the effect of temperature increases with increasing Pd composition. However, at these compositions relevant to SAAs, the changes in the percentage of the surface that is Pd are all relatively small (<5%) over a large temperature range, suggesting that under vacuum, changes in temperature will result in minimal restructuring of the nanoparticles. The MC results for the CS-based model yield almost identical patterns, with the percentage of the surface that is Pd being slightly less than that predicted with the bond-energy model.

4. CONCLUSIONS

Here, we use 201-atom nanoparticle models to predict the structures of AuPd alloys. Exchanging Pd into Au nanoparticles becomes more exothermic with an increasing coordination of

the exchange site. This suggests that Pd prefers to be in the subsurface of the nanoparticle. Similarly, exchange energies increase linearly with the number of Pd neighbors at the exchange site, suggesting that Pd prefers to be isolated from itself within Au. Pd's affinity for the subsurface and isolation from itself agrees with prior literature. Pd in next-nearest neighbor positions to the exchange site is less influential on the exchange energies but does still weakly penalize exchange, affirming that Pd prefers to be well isolated from other Pd atoms within these nanoparticles.

Investigating the effects of Pd in the remainder of the nanoparticles (at positions far from the exchange site), we observe nonlinear changes in exchange energies with increasing Pd in the extended nanoparticle. Most notably, there is a large difference (~ 20 kJ mol⁻¹) in adding Pd to an Au₁₉₁Pd₁₀ nanoparticle than to an Au₁₉₀Pd₁₁ particle, even if the exchange site does not change and the number of Pd neighbors around the exchange site does not change. Adding one additional Pd to the nanoparticle, far from the exchange site, results in a large jump in the exchange energies. These nonlinear effects are shown to be caused by changes in the Fermi level of the AuPd nanoparticle with composition.

Many models have been developed and used to predict energies and structures of AuPd alloys, including bond-energy-based models, machine-learning-based neural networks, cluster-expansion models, and force-field-based embedded atom models. Among these, bond-energy models are attractive in their simplicity but had not yet been adapted or assessed for nanoparticle AuPd alloys. Thus, we modified and regressed two models using the DFT data. One model (CS-based) perturbs infinite-dilution exchange energies based on the number of Pd near the exchange site for higher Pd compositions, resulting in 12 calculated and 3 regressed parameters. The other model (bond-energy-based) assigns energies to each type of bond based on composition (Au–Au, Au–Pd, or Pd–Pd) and site-type (e.g., subsurface or corner), resulting in 50 regressed parameters. Both models account for changes in the Fermi level of the nanoparticle to address the nonlinear effects described above. Between these two models, the CS-based model has an MAE value of 3.9 kJ mol⁻¹, while the bond-energy model has an MAE value of 3.4 kJ mol⁻¹ when compared to the DFT-calculated exchange energies used to train the models. These errors are similar to those reported using other approaches (e.g., cluster expansion models) that generally require more regressed parameters and thus more DFT data in the training set.

MC simulations yield similar results for both models for Au-rich nanoparticles (Au/Pd > 1). The simulations predict that nearly all the Pd will remain in the subsurface of the particle until roughly half the subsurface is filled, at which point Pd will start to populate surface sites. Pd will primarily form monomers on the surface at lower Pd (<25 mol %) contents, but Pd dimers will quickly form at higher Pd contents, and at 55 mol % Pd, essentially all Pd will be present in dimers (80% of surface ensembles). The composition at which Pd starts to populate the surface and form multinuclear ensembles will depend on the relative size of the surface compared to the subsurface (i.e., the nanoparticle size and shape). While these insights reflect a baseline expectation of catalyst structure, the arrangement of Pd within the nanoparticle will also be sensitive to surface-bound species (e.g., CO*, O*) that may be present during reaction or catalyst characterizations. The impacts of nanoparticle size and shape, as well as surface restructuring

caused by contacting gases, will be enabled in future studies by the methodological framework developed here, combining DFT, MC, and bond-energy models.

■ ASSOCIATED CONTENT

Supporting Information

The Supporting Information is available free of charge at <https://pubs.acs.org/doi/10.1021/acs.jpcc.4c08571>.

Monte Carlo simulations and the 201-atom particle model (Section S1), the effects of increasing Pd content at various locations in the particle on exchange energies (Section S2), and the parametrized models investigated in this work (Section S3) (PDF)

Monte Carlo simulations within the Computational Catalysis Interface (CCI) (TXT)

■ AUTHOR INFORMATION

Corresponding Author

David Hibbitts – Department of Chemical Engineering, University of Florida, Gainesville, Florida 32608, United States; Present Address: Charles D. Davidson School of Chemical Engineering, Purdue University, West Lafayette, Indiana, 47907, United States; orcid.org/0000-0001-8606-7000; Email: hibbitts@purdue.edu

Authors

Conor Waldt – Department of Chemical Engineering, University of Florida, Gainesville, Florida 32608, United States; Present Address: Charles D. Davidson School of Chemical Engineering, Purdue University, West Lafayette, Indiana, 47907, United States

Rajeev Kumar – Department of Chemical Engineering, University of Florida, Gainesville, Florida 32608, United States; Present Address: Charles D. Davidson School of Chemical Engineering, Purdue University, West Lafayette, Indiana, 47907, United States

Complete contact information is available at: <https://pubs.acs.org/10.1021/acs.jpcc.4c08571>

Notes

The authors declare no competing financial interest.

■ ACKNOWLEDGMENTS

We would like to express our gratitude to the National Science Foundation (NSF, grant number 2300020) for financial support and for computational resources (via ACCESS).

■ REFERENCES

- (1) Hannagan, R. T.; Giannakakis, G.; Flytzani-Stephanopoulos, M.; Sykes, E. C. H. Single-Atom Alloy Catalysis. *Chem. Rev.* **2020**, *120*, 12044–12088.
- (2) Han, J.; Lu, J.; Wang, M.; Wang, Y.; Wang, F. Single Atom Alloy Preparation and Applications in Heterogeneous Catalysis. *Chin. J. Chem.* **2019**, *37*, 977–988.
- (3) Giannakakis, G.; Flytzani-Stephanopoulos, M.; Sykes, E. C. H. Single-Atom Alloys as a Reductionist Approach to the Rational Design of Heterogeneous Catalysts. *Acc. Chem. Res.* **2019**, *52*, 237–247.
- (4) Darby, M. T.; Stamatakis, M.; Michaelides, A.; Sykes, E. C. H. Lonely Atoms with Special Gifts: Breaking Linear Scaling Relationships in Heterogeneous Catalysis with Single-Atom Alloys. *J. Phys. Chem. Lett.* **2018**, *9*, 5636–5646.

- (5) Kyriakou, G.; Boucher, M. B.; Jewell, A. D.; Lewis, E. A.; Lawton, T. J.; Baber, A. E.; Tierney, H. L.; Flytzani-Stephanopoulos, M.; Sykes, E. C. H. Isolated Metal Atom Geometries as a Strategy for Selective Heterogeneous Hydrogenations. *Science* **2012**, *335*, 1209–1212.
- (6) Liu, J.; Uhlman, M. B.; Montemore, M. M.; Trimpalis, A.; Giannakakis, G.; Shan, J.; Cao, S.; Hannagan, R. T.; Sykes, E. C. H.; Flytzani-Stephanopoulos, M. Integrated Catalysis-Surface Science-Theory Approach to Understand Selectivity in the Hydrogenation of 1-Hexyne to 1-Hexene on PdAu Single-Atom Alloy Catalysts. *ACS Catal.* **2019**, *9*, 8757–8765.
- (7) Thirumalai, H.; Kitchin, J. R. Investigating the Reactivity of Single Atom Alloys Using Density Functional Theory. *Top. Catal.* **2018**, *61*, 462–474.
- (8) Pei, G. X.; Liu, X. Y.; Wang, A.; Li, L.; Huang, Y.; Zhang, T.; Lee, J. W.; Jang, B. W. L.; Mou, C.-Y. Promotional Effect of Pd Single Atoms on Au Nanoparticles Supported on Silica for the Selective Hydrogenation of Acetylene in Excess Ethylene. *New J. Chem.* **2014**, *38*, 2043.
- (9) Liu, J.; Shan, J.; Lucci, F. R.; Cao, S.; Sykes, E. C. H.; Flytzani-Stephanopoulos, M. Palladium–Gold Single Atom Alloy Catalysts for Liquid Phase Selective Hydrogenation of 1-Hexyne. *Catal. Sci. Technol.* **2017**, *7*, 4276–4284.
- (10) Hayashi, S.; Ishida, R.; Hasegawa, S.; Yamazoe, S.; Tsukuda, T. Doping a Single Palladium Atom into Gold Superatoms Stabilized by PVP: Emergence of Hydrogenation Catalysis. *Top. Catal.* **2017**, *61*, 1–6.
- (11) Luneau, M.; Shirman, T.; Foucher, A. C.; Duanmu, K.; Verbart, D. M. A.; Sautet, P.; Stach, E. A.; Aizenberg, J.; Madix, R. J.; Friend, C. M. Achieving High Selectivity for Alkyne Hydrogenation at High Conversions with Compositionally Optimized PdAu Nanoparticle Catalysts in Raspberry Colloid-Templated SiO₂. *ACS Catal.* **2020**, *10*, 441–450.
- (12) Aich, P.; Wei, H.; Basan, B.; Kropf, A. J.; Schweitzer, N. M.; Marshall, C. L.; Miller, J. T.; Meyer, R. Single-Atom Alloy Pd–Ag Catalyst for Selective Hydrogenation of Acrolein. *J. Phys. Chem. C* **2015**, *119*, 18140–18148.
- (13) Zhang, S.; Chen, C.-Y.; Jang, B. W.-L.; Zhu, A.-M. Radio-Frequency H₂ Plasma Treatment of AuPd/TiO₂ Catalyst for Selective Hydrogenation of Acetylene in Excess Ethylene. *Catal. Today* **2015**, *256*, 161–169.
- (14) Luneau, M.; Guan, E.; Chen, W.; Foucher, A. C.; Marcella, N.; Shirman, T.; Verbart, D. M. A.; Aizenberg, J.; Aizenberg, M.; Stach, E. A.; et al. Enhancing Catalytic Performance of Dilute Metal Alloy Nanomaterials. *Commun. Chem.* **2020**, *3* (1), 46.
- (15) Boucher, M. B.; Zugic, B.; Cladaras, G.; Kammert, J.; Marcinkowski, M. D.; Lawton, T. J.; Sykes, E. C. H.; Flytzani-Stephanopoulos, M. Single Atom Alloy Surface Analogs in Pd_{0.18}Cu_{0.15} Nanoparticles for Selective Hydrogenation Reactions. *Phys. Chem. Chem. Phys.* **2013**, *15*, 12187–12196.
- (16) Zhu, M.-M.; Du, X.-L.; Zhao, Y.; Mei, B.-B.; Zhang, Q.; Sun, F.-F.; Jiang, Z.; Liu, Y.-M.; He, H.-Y.; Cao, Y. Ring-Opening Transformation of 5-Hydroxymethylfurfural Using a Golden Single-Atomic-Site Palladium Catalyst. *ACS Catal.* **2019**, *9*, 6212–6222.
- (17) Seemala, B.; Cai, C. M.; Wyman, C. E.; Christopher, P. Support Induced Control of Surface Composition in Cu–Ni/TiO₂ Catalysts Enables High Yield Co-Conversion of HMF and Furfural to Methylated Furans. *ACS Catal.* **2017**, *7*, 4070–4082.
- (18) Seemala, B.; Cai, C. M.; Kumar, R.; Wyman, C. E.; Christopher, P. Effects of Cu–Ni Bimetallic Catalyst Composition and Support on Activity, Selectivity, and Stability for Furfural Conversion to 2-Methylfuran. *ACS Sustainable Chem. Eng.* **2018**, *6*, 2152–2161.
- (19) Chia, M.; Pagán-Torres, Y. J.; Hibbitts, D.; Tan, Q.; Pham, H. N.; Datye, A. K.; Neurock, M.; Davis, R. J.; Dumesic, J. A. Selective Hydrogenolysis of Polyols and Cyclic Ethers over Bifunctional Surface Sites on Rhodium-Rhenium Catalysts. *J. Am. Chem. Soc.* **2011**, *133*, 12675–12689.
- (20) Sun, G.; Zhao, Z.-J.; Mu, R.; Zha, S.; Li, L.; Chen, S.; Zang, K.; Luo, J.; Li, Z.; Purdy, S. C.; et al. Breaking the Scaling Relationship via Thermally Stable Pt/Cu Single Atom Alloys for Catalytic Dehydrogenation. *Nat. Commun.* **2018**, *9* (1), 4454.
- (21) Shan, J.; Lucci, F. R.; Liu, J.; El-Soda, M.; Marcinkowski, M. D.; Allard, L. F.; Sykes, E. C. H.; Flytzani-Stephanopoulos, M. Water Co-Catalyzed Selective Dehydrogenation of Methanol to Formaldehyde and Hydrogen. *Surf. Sci.* **2016**, *650*, 121–129.
- (22) Shan, J.; Liu, J.; Li, M.; Lustig, S.; Lee, S.; Flytzani-Stephanopoulos, M. NiCu Single Atom Alloys Catalyze the C H Bond Activation in the Selective Non-Oxidative Ethanol Dehydrogenation Reaction. *Appl. Catal., B* **2018**, *226*, 534–543.
- (23) Yu, W.-Y.; Mullen, G. M.; Flaherty, D. W.; Mullins, C. B. Selective Hydrogen Production from Formic Acid Decomposition on Pd–Au Bimetallic Surfaces. *J. Am. Chem. Soc.* **2014**, *136*, 11070–11078.
- (24) Li, H.; Henkelman, G. Dehydrogenation Selectivity of Ethanol on Close-Packed Transition Metal Surfaces: A Computational Study of Monometallic, Pd/Au, and Rh/Au Catalysts. *J. Phys. Chem. C* **2017**, *121*, 27504–27510.
- (25) Li, H.; Chai, W.; Henkelman, G. Selectivity for Ethanol Partial Oxidation: The Unique Chemistry of Single-Atom Alloy Catalysts on Au, Ag, and Cu(111). *J. Mater. Chem. A* **2019**, *7*, 23868–23877.
- (26) Chang, C.-R.; Long, B.; Yang, X.-F.; Li, J. Theoretical Studies on the Synergetic Effects of Au–Pd Bimetallic Catalysts in the Selective Oxidation of Methanol. *J. Phys. Chem. C* **2015**, *119*, 16072–16081.
- (27) Li, H.; Evans, E. J.; Mullins, C. B.; Henkelman, G. Ethanol Decomposition on Pd–Au Alloy Catalysts. *J. Phys. Chem. C* **2018**, *122*, 22024–22032.
- (28) Evans, E. J.; Li, H.; Yu, W.-Y.; Mullen, G. M.; Henkelman, G.; Mullins, C. B. Mechanistic Insights on Ethanol Dehydrogenation on Pd–Au Model Catalysts: A Combined Experimental and DFT Study. *Phys. Chem. Chem. Phys.* **2017**, *19*, 30578–30589.
- (29) Wang, Z.-T.; Hoyt, R. A.; El-Soda, M.; Madix, R. J.; Kaxiras, E.; Sykes, E. C. H. Dry Dehydrogenation of Ethanol on Pt–Cu Single Atom Alloys. *Top. Catal.* **2017**, *61*, 1–8.
- (30) Boucher, M. B.; Marcinkowski, M. D.; Liriano, M. L.; Murphy, C. J.; Lewis, E. A.; Jewell, A. D.; Mattera, M. F. G.; Kyriakou, G.; Flytzani-Stephanopoulos, M.; Sykes, E. C. H. Molecular-Scale Perspective of Water-Catalyzed Methanol Dehydrogenation to Formaldehyde. *ACS Nano* **2013**, *7*, 6181–6187.
- (31) Darby, M. T.; Réocreux, R.; Sykes, E.; Charles, H.; Michaelides, A.; Stamatakis, M. Elucidating the Stability and Reactivity of Surface Intermediates on Single-Atom Alloy Catalysts. *ACS Catal.* **2018**, *8* (6), 5038–5050.
- (32) Giannakakis, G.; Trimpalis, A.; Shan, J.; Qi, Z.; Cao, S.; Liu, J.; Ye, J.; Biener, J.; Flytzani-Stephanopoulos, M. NiAu Single Atom Alloys for the Non-Oxidative Dehydrogenation of Ethanol to Acetaldehyde and Hydrogen. *Top. Catal.* **2018**, *61*, 475–486.
- (33) Zhang, M.; Yang, B.; Yu, Y. A Density Functional Theory Study on the Conversion of Ethylene to Carbon Monomer on PdAu(1 0 0) Surface. *Appl. Surf. Sci.* **2015**, *356*, 1252–1261.
- (34) Réocreux, R.; Uhlman, M.; Thuening, T.; Kress, P.; Hannagan, R.; Stamatakis, M.; Sykes, E. C. H. Efficient and Selective Carbon–Carbon Coupling on Coke-Resistant PdAu Single-Atom Alloys. *Chem. Commun.* **2019**, *55*, 15085–15088.
- (35) Trimpalis, A.; Giannakakis, G.; Cao, S.; Flytzani-Stephanopoulos, M. NiAu Single Atom Alloys for the Selective Oxidation of Methacrolein with Methanol to Methyl Methacrylate. *Catal. Today* **2019**, *355*, 804–814.
- (36) Chen, F.; Jiang, X.; Zhang, L.; Lang, R.; Qiao, B. Single-Atom Catalysis: Bridging the Homo- and Heterogeneous Catalysis. *Chin. J. Catal.* **2018**, *39*, 893–898.
- (37) Zhang, L.; Wang, A.; Miller, J. T.; Liu, X.; Yang, X.; Wang, W.; Li, L.; Huang, Y.; Mou, C.-Y.; Zhang, T. Efficient and Durable Au Alloyed Pd Single-Atom Catalyst for the Ullmann Reaction of Aryl Chlorides in Water. *ACS Catal.* **2014**, *4*, 1546–1553.
- (38) Chen, M.; Kumar, D.; Yi, C.-W.; Goodman, D. W. The Promotional Effect of Gold in Catalysis by Palladium–Gold. *Science* **2005**, *310*, 291–293.

- (39) Yu, W.-Y.; Zhang, L.; Mullen, G. M.; Henkelman, G.; Mullins, C. B. Oxygen Activation and Reaction on Pd–Au Bimetallic Surfaces. *J. Phys. Chem. C* **2015**, *119*, 11754–11762.
- (40) Ham, H. C.; Hwang, G. S.; Han, J.; Yoon, S. P.; Nam, S. W.; Lim, T. H. Importance of Pd Monomer Pairs in Enhancing the Oxygen Reduction Reaction Activity of the AuPd(1 0 0) Surface: A First Principles Study. *Catal. Today* **2016**, *263*, 11–15.
- (41) Yuan, D. W.; Liu, Z. R.; Xu, Y. First-Principles Investigations of O₂ Dissociation on Low-Coordinated Pd Ensembles over Stepped Au Surfaces. *Phys. Lett. A* **2012**, *376*, 3432–3438.
- (42) Yuan, D. W.; Liu, Z. R.; Chen, J. H. Catalytic Activity of Pd Ensembles over Au(111) Surface for CO Oxidation: A First-Principles Study. *J. Chem. Phys.* **2011**, *134* (5), 054704.
- (43) Luneau, M.; Shirman, T.; Filie, A.; Timoshenko, J.; Chen, W.; Trimpalis, A.; Flytzani-Stephanopoulos, M.; Kaxiras, E.; Frenkel, A. I.; Aizenberg, J.; et al. Dilute Pd/Au Alloy Nanoparticles Embedded in Colloid-Templated Porous SiO₂: Stable Au-Based Oxidation Catalysts. *Chem. Mater.* **2019**, *31*, 5759–5768.
- (44) Gao, F.; Wang, Y.; Goodman, D. W. CO Oxidation over AuPd(100) from Ultrahigh Vacuum to near-Atmospheric Pressures: The Critical Role of Contiguous Pd Atoms. *J. Am. Chem. Soc.* **2009**, *131*, 5734–5735.
- (45) Williams, C.; Carter, J. H.; Dummer, N. F.; Chow, Y. K.; Morgan, D. J.; Jacob, S.; Serna, P.; Willock, D. J.; Meyer, R. J.; Taylor, S. H.; et al. Selective Oxidation of Methane to Methanol Using Supported AuPd Catalysts Prepared by Stabilizer-Free Sol-Immobilization. *ACS Catal.* **2018**, *8*, 2567–2576.
- (46) Huang, X.; Akdim, O.; Douthwaite, M.; Wang, K.; Zhao, L.; Lewis, R. J.; Pattison, S.; Daniel, I. T.; Miedziak, P. J.; Shaw, G.; et al. Au–Pd Separation Enhances Bimetallic Catalysis of Alcohol Oxidation. *Nature* **2022**, *603*, 271–275.
- (47) Ricciardulli, T.; Gorthy, S.; Adams, J. S.; Thompson, C.; Karim, A. M.; Neurock, M.; Flaherty, D. W. Effect of Pd Coordination and Isolation on the Catalytic Reduction of O₂ to H₂O₂ over PdAu Bimetallic Nanoparticles. *J. Am. Chem. Soc.* **2021**, *143*, 5445–5464.
- (48) Jirkovský, J. S.; Panas, I.; Ahlberg, E.; Halasa, M.; Romani, S.; Schiffrin, D. J. Single Atom Hot-Spots at Au–Pd Nanoparticles for Electrocatalytic H₂O₂ Production. *J. Am. Chem. Soc.* **2011**, *133*, 19432–19441.
- (49) Wrasman, C. J.; Boubnov, A.; Riscoe, A. R.; Hoffman, A. S.; Bare, S. R.; Cargnello, M. Synthesis of Colloidal Pd/Au Dilute Alloy Nanocrystals and Their Potential for Selective Catalytic Oxidations. *J. Am. Chem. Soc.* **2018**, *140*, 12930–12939.
- (50) Todorovic, R.; Meyer, R. J. A Comparative Density Functional Theory Study of the Direct Synthesis of H₂O₂ on Pd, Pt and Au Surfaces. *Catal. Today* **2011**, *160*, 242–248.
- (51) Svensson, R.; Grönbeck, H. Site Communication in Direct Formation of H₂O₂ over Single-Atom Pd@Au Nanoparticles. *J. Am. Chem. Soc.* **2023**, *145*, 11579–11588.
- (52) Ham, H. C.; Stephens, J. A.; Hwang, G. S.; Han, J.; Nam, S. W.; Lim, T. H. Pd Ensemble Effects on Oxygen Hydrogenation in AuPd Alloys: A Combined Density Functional Theory and Monte Carlo Study. *Catal. Today* **2011**, *165*, 138–144.
- (53) Ouyang, M.; Papanikolaou, K. G.; Boubnov, A.; Hoffman, A. S.; Giannakakis, G.; Bare, S. R.; Stamatakis, M.; Flytzani-Stephanopoulos, M.; Sykes, E. C. H. Directing Reaction Pathways via in Situ Control of Active Site Geometries in PdAu Single-Atom Alloy Catalysts. *Nat. Commun.* **2021**, *12* (1), 1549.
- (54) Boscoboinik, J. A.; Plaisance, C.; Neurock, M.; Tysoe, W. T. Monte Carlo and Density Functional Theory Analysis of the Distribution of Gold and Palladium Atoms Onalloys. *Phys. Rev. B* **2008**, *77*, 045422.
- (55) Wei, T.; Wang, J.; Goodman, D. W. Characterization and Chemical Properties of Pd–Au Alloy Surfaces†. *J. Phys. Chem. C* **2007**, *111*, 8781–8788.
- (56) Abbott, H. L.; Aumer, A.; Lei, Y.; Asokan, C.; Meyer, R. J.; Sterrer, M.; Shaikhutdinov, S.; Freund, H. J. CO Adsorption on Monometallic and Bimetallic Au–Pd Nanoparticles Supported on Oxide Thin Films. *J. Phys. Chem. C* **2010**, *114*, 17099–17104.
- (57) Gibson, E. K.; Beale, A. M.; Catlow, C. R. A.; Chutia, A.; Gianolio, D.; Gould, A.; Kroner, A.; Mohammed, K. M. H.; Perdjon, M.; Rogers, S. M.; et al. Restructuring of AuPd Nanoparticles Studied by a Combined XAFS/DRIFTS Approach. *Chem. Mater.* **2015**, *27*, 3714–3720.
- (58) Liu, H. B.; Pal, U.; Medina, A.; Maldonado, C.; Ascencio, J. A. Structural Incoherency And Structure Reversal In Bimetallicnanoclusters. *Phys. Rev. B* **2005**, *71*, 075403.
- (59) Ferrando, R.; Jellinek, J.; Johnston, R. L. Nanoalloys: From Theory to Applications of Alloy Clusters and Nanoparticles. *Chem. Rev.* **2008**, *108*, 845–910.
- (60) Ter-Oganessian, N. V.; Rusalev, Y. V.; Motseyko, A. V.; Guda, A. A.; Soldatov, A. V. Stability and Phase Transformations in Au–Pd Nanoparticles Studied by Means of Combined Monte Carlo and Molecular Dynamics Simulations. *J. Phys. Chem. C* **2024**, *128*, 3054–3063.
- (61) Rahm, J. M.; Erhart, P. Understanding Chemical Ordering in Bimetallic Nanoparticles from Atomic-Scale Simulations: The Competition between Bulk, Surface, and Strain. *J. Phys. Chem. C* **2018**, *122*, 28439–28445.
- (62) Marchal, R.; Genest, A.; Krüger, S.; Rösch, N. Structure of Pd/Au Alloy Nanoparticles from a Density Functional Theory-Based Embedded-Atom Potential. *J. Phys. Chem. C* **2013**, *117*, 21810–21822.
- (63) Zhu, B.; Thrimurthulu, G.; Delannoy, L.; Louis, C.; Mottet, C.; Creuze, J.; Legrand, B.; Guesmi, H. Evidence of Pd Segregation and Stabilization at Edges of AuPd Nano-Clusters in the Presence of CO: A Combined DFT and DRIFTS Study. *J. Catal.* **2013**, *308*, 272–281.
- (64) Bruma, A.; Ismail, R.; Paz-Borbón, L. O.; Arslan, H.; Barcaro, G.; Fortunelli, A.; Li, Z. Y.; Johnston, R. L. DFT Study of the Structures and Energetics of 98-Atom AuPd Clusters. *Nanoscale* **2013**, *5* (2), 646–652.
- (65) Atanasov, I.; Hou, M. Equilibrium Ordering Properties of Au–Pd Alloys and Nanoalloys. *Surf. Sci.* **2009**, *603*, 2639–2651.
- (66) Yudanov, I. V.; Neyman, K. M. Stabilization of Au at Edges of Bimetallic PdAu Nanocrystallites. *Phys. Chem. Chem. Phys.* **2010**, *12*, 5094–5100.
- (67) Zhu, B.; Creuze, J.; Mottet, C.; Legrand, B.; Guesmi, H. CO Adsorption-Induced Surface Segregation and Formation of Pd Chains on AuPd(100) Alloy: Density Functional Theory Based Ising Model and Monte Carlo Simulations. *J. Phys. Chem. C* **2016**, *120*, 350–359.
- (68) Li, L.; Li, X.; Duan, Z.; Meyer, R. J.; Carr, R.; Raman, S.; Kozioł, L.; Henkelman, G. Adaptive Kinetic Monte Carlo Simulations of Surface Segregation in PdAu Nanoparticles. *Nanoscale* **2019**, *11*, 10524–10535.
- (69) Boes, J. R.; Kitchin, J. R. Modeling Segregation on AuPd(111) Surfaces with Density Functional Theory and Monte Carlo Simulations. *J. Phys. Chem. C* **2017**, *121*, 3479–3487.
- (70) Stephens, J. A.; Hwang, G. S. Atomic Arrangements in AuPt/Pt(100) and AuPd/Pd(100) Surface Alloys: A Monte Carlo Study Using First Principles-Based Cluster Expansions. *J. Phys. Chem. C* **2011**, *115*, 21205–21210.
- (71) Mueller, T. Ab Initio Determination of Structure-Property Relationships in Alloy Nanoparticles. *Phys. Rev. B* **2012**, *86*, 144201.
- (72) Papanikolaou, K. G.; Darby, M. T.; Stamatakis, M. Engineering the Surface Architecture of Highly Dilute Alloys: An Ab Initio Monte Carlo Approach. *ACS Catal.* **2020**, *10*, 1224–1236.
- (73) Stephens, J. A.; Ham, H. C.; Hwang, G. S. Atomic Arrangements of AuPt/Pt(111) and AuPd/Pd(111) Surface Alloys: A Combined Density Functional Theory and Monte Carlo Study. *J. Phys. Chem. C* **2010**, *114*, 21516–21523.
- (74) Kravchenko, P.; Plaisance, C.; Hibbits, D. A New Computational Interface for Catalysis. *ChemRxiv* **2019**.
- (75) Kresse, G.; Furthmüller, J. Efficiency of Ab-Initio Total Energy Calculations for Metals and Semiconductors Using a Plane-Wave Basis Set. *Comput. Mater. Sci.* **1996**, *6*, 15–50.
- (76) Kresse, G.; Furthmüller, J. Efficient Iterative Schemes for Ab Initio Total-Energy Calculations Using a Plane-Wave Basis Set. *Phys. Rev. B* **1996**, *54*, 11169–11186.

- (77) Kresse, G.; Hafner, J. Ab Initio Molecular Dynamics for Open-Shell Transition Metals. *Phys. Rev. B: condens. Matter* **1993**, *48*, 13115–13118.
- (78) Kresse, G.; Hafner, J. Ab Initio Molecular-Dynamics Simulation of the Liquid-Metal-Amorphous-Semiconductor Transition in Germanium. *Phys. Rev. B* **1994**, *49*, 14251–14269.
- (79) Kresse, G.; Joubert, D. From Ultrasoft Pseudopotentials to the Projector Augmented-Wave Method. *Phys. Rev. B* **1999**, *59*, 1758–1775.
- (80) Blöchl, P. E. Projector Augmented-Wave Method. *Phys. Rev. B* **1994**, *50*, 17953–17979.
- (81) Hammer, B.; Hansen, L. B.; Nørskov, J. K. Improved Adsorption Energetics within Density-Functional Theory Using Revised Perdew-Burke-Ernzerhof Functionals. *Phys. Rev. B* **1999**, *59*, 7413–7421.
- (82) Perdew, J. P.; Burke, K.; Ernzerhof, M. Generalized Gradient Approximation Made Simple. *Phys. Rev. Lett.* **1996**, *77*, 3865–3868.
- (83) Zhang, Y.; Yang, W. Comment on “Generalized Gradient Approximation Made Simple”. *Phys. Rev. Lett.* **1998**, *80*, 890–890.
- (84) Grimme, S. Semiempirical GGA-Type Density Functional Constructed with a Long-Range Dispersion Correction. *J. Comput. Chem.* **2006**, *27*, 1787–1799.
- (85) Grimme, S.; Ehrlich, S.; Goerigk, L. Effect of the Damping Function in Dispersion Corrected Density Functional Theory. *J. Comput. Chem.* **2011**, *32*, 1456–1465.
- (86) Perdew, J. P.; Ruzsinszky, A.; Csonka, G. I.; Vydrov, O. A.; Scuseria, G. E.; Constantin, L. A.; Zhou, X.; Burke, K. Restoring the Density-Gradient Expansion for Exchange in Solids and Surfaces. *Phys. Rev. Lett.* **2008**, *100*, 136406.
- (87) Dion, M.; Rydberg, H.; Schröder, E.; Langreth, D. C.; Lundqvist, B. I. Van Der Waals Density Functional for General Geometries. *Phys. Rev. Lett.* **2004**, *92*, 246401.
- (88) Román-Pérez, G.; Soler, J. M. Efficient Implementation of a van Der Waals Density Functional: Application to Double-Wall Carbon Nanotubes. *Phys. Rev. Lett.* **2009**, *103*, 096102.
- (89) Klimeš, J.; Bowler, D. R.; Michaelides, A. Van Der Waals Density Functionals Applied to Solids. *Phys. Rev. B* **2011**, *83*, 195131.
- (90) Klimeš, J.; Bowler, D. R.; Michaelides, A. Chemical Accuracy for the van Der Waals Density Functional. *J. Phys.: condens. Matter* **2010**, *22*, 022201.
- (91) Lee, K.; Murray, É. D.; Kong, L.; Lundqvist, B. I.; Langreth, D. C. Higher-Accuracy van Der Waals Density Functional. *Phys. Rev. B* **2010**, *82*, 081101.
- (92) Wang, G.; Xu, Y.-S.; Qian, P.; Su, Y.-J. The Effects of Size and Shape on the Structural and Thermal Stability of Platinum Nanoparticles. *Comput. Mater. Sci.* **2019**, *169*, 109090.
- (93) Bao, K.; Goedecker, S.; Koga, K.; Lançon, F.; Neelov, A. Structure of Large Gold Clusters Obtained by Global Optimization Using the Minima Hopping Method. *Phys. Rev. B* **2009**, *79*, 041405.
- (94) Garden, A. L.; Pedersen, A.; Jónsson, H. Reassignment of “magic Numbers” for Au Clusters of Decahedral and FCC Structural Motifs. *Nanoscale* **2018**, *10*, 5124–5132.
- (95) Wei, X.; Shao, B.; Zhou, Y.; Li, Y.; Jin, C.; Liu, J.; Shen, W. Geometrical Structure of the Gold-Iron(III) Oxide Interfacial Perimeter for CO Oxidation. *Angew. Chem. Int. Ed.* **2018**, *57*, 11289–11293.
- (96) Mejía-Rosales, S. J.; Fernández-Navarro, C.; Pérez-Tijerina, E.; Blom, D. A.; Allard, L. F.; José-Yacamán, M. On the Structure of Au/Pd Bimetallic Nanoparticles. *J. Phys. Chem. C* **2007**, *111*, 1256–1260.